International Journal of Mechanical Sciences 300 (2025) 110381

Contents lists available at ScienceDirect

International Journal of Mechanical Sciences

journal homepage: www.elsevier.com/locate/ijmecsci

H_∞ optimization of a hybrid multiple-delayed delayed resonator vibration absorber

Yifan Liu [a], Bo Yan [b], Li Cheng [a,*]

[a] Department of Mechanical Engineering, The Hong Kong Polytechnic University, Hong Kong, China
[b] School of Mechanical Engineering, Zhejiang Sci-Tech University, Hangzhou, China

ARTICLE INFO

Keywords:
Active vibration control
Multiple-delayed system
H_∞ optimization
Delayed resonator
Resonance and antiresonance

ABSTRACT

Delayed resonator (DR) as an active vibration absorber can achieve a zero antiresonance point of the primary structure at a given frequency by manipulating the loop delay, yielding the so-called complete vibration suppression. Achieving zero antiresonance, however, is usually penalized by the significantly raised resonance peaks, risking structural safety. Here, we aim to limit the resonance while achieving zero antiresonance, leading to the H_∞ optimization problem. To simplify analyses, we distinctively incorporate the primary structure-based feedback force into the total control forces of the DR and activate them only when residual vibrations occur. This reduces parametric coupling so that resonance peaks can be reduced without affecting zero antiresonance. Given the benefits of tuning delay from the DR concept itself, the states of the primary structure are also delayed in the feedback loop for additional performance enhancement, finally creating the so-called hybrid multiple-delayed DR. By analyzing system stability, characteristic spectrum, and frequency response, we show that pursuing an extremum reduction of resonance peaks can conflict with operable complete vibration suppression, thus requiring a trade-off between the two. Furthermore, by properly optimizing control parameters, both tasks can be significantly enhanced simultaneously. This work introduces a new design framework to enhance vibration suppression in terms of both resonance and antiresonance.

1. Introduction

Dynamic vibration absorber (DVA) as a simple yet effective vibration reduction technique has been extensively investigated since its invention by Frahm [1] in the 1900s. This work focuses on the delayed resonator (DR), a type of active DVA proposed by Olgac et al. [2–5] to achieve complete vibration suppression at a given frequency by introducing proper time delays into the feedback loop. The known benefits of manipulating delay include increasing the number of tunable control parameters without increasing control terms for stronger robustness [6], modeling the inevitable loop delays for a more accurate dynamical prediction and thus better vibration suppression, posing no requirements on system states for tuning control forces thus facilitating sensor uses [7], etc. The DR has a wide range of potential engineering applications [8], e.g., vibration control of helicopter fuselages, gearboxes, and machining chatter, etc. The development of DR has also experienced a booming increase since its invention, making it a critical tributary of DVAs and a typical counter-intuitive example that larger delays can enhance control performance.

Among the prosperous research over the past decade, Nia and Sipahi [9] designed a delay-independent control law to enhance robustness against delay perturbations. Vyhlídal et al. [10] proposed spectral methods to address stability issues. Sun and Xu [11,12] identified and then increased the loop delay to enhance vibration suppression. Kammer and Olgac [13] and Karama et al. [14] sensitized system responses by tuning delays to harvest energy while suppressing vibrations. Pilbauer et al. [15], Kučera et al. [16], and Liu et al. [17] adopted distributed-delayed control laws to reduce the effects of measurement noises, see also [18] for optimizing the delay distribution to handle a small frequency mismatch. Eris et al. [19] optimized system spectra to expedite responses. Zhang et al. [20] and Sinou et al. [21] modeled friction effects when tuning DR. Cai et al. [22,23] unified the tuning mechanism when incorporating different feedback states using the fractional-order operator. Kuře et al. [24] extended the antiresonance valley by assigning double imaginary roots to the DR subsystem. Šika et al. [25–27] achieved multiple-directional complete vibration suppression in robotic applications. In addition, the DR was tuned to resonate a multiple-degree-of-freedom (MDOF) structure as the absorber so that the force actuator can be installed independent of the position of the primary structure alongside the reduction of the absorber vibrations [28–31]. One also can refer to [32–38] for combining the benefits of delayed control with mechanical advantages

* Corresponding author.
E-mail address: li.cheng@polyu.edu.hk (L. Cheng).

https://doi.org/10.1016/j.ijmecsci.2025.110381
Received 12 December 2024; Received in revised form 14 April 2025; Accepted 14 May 2025
Available online 27 May 2025

to enhance vibration suppression. We point out that active control (not necessarily delayed control) has been increasingly applied to enhance vibration reduction to meet higher or customized demands of modern equipment or structures, as evidenced by [39–42], see also [43–45] for the vibration absorber design in various forms.

A tuned DR achieves complete vibration suppression by creating a zero antiresonance at the specified tuning frequency on the frequency response curve of the primary structure, which, however, can significantly raise the resonance peaks compared with the passive case. Given that perturbations are inevitable in practice, such a DR amplifies the maximum possible vibrations on primary structures, thus defeating the original purpose of vibration reduction. Note that the consequences of a resonant primary structure can be catastrophic even if the exciting perturbation is small and lasts shortly [46]. Though briefly mentioned in the previous work [22], effective ways to limit the raised resonance peaks when implementing DRs are still a research gap.

On the other hand, the criterion of minimizing the resonant or maximum (H_∞ norm) vibration amplitude of a primary structure has been extensively applied to the structural design of passive DVAs, yielding the so-called H_∞ optimization [47,48], the long history of which has been well documented in [49–55] and the references therein. Meanwhile, such an optimization criterion has also been generalized to the design of active DVAs. For instance, Chatterjee [56] optimized a PD-controlled DVA, resulting in significantly reduced resonance peaks compared to a passive DVA using optimum structural parameters. Cheung et al. [57] optimized both structural and control parameters so that good vibration reduction can be achieved with a small absorber mass. Li et al. [58] proposed and optimized a PID-controlled DVA without needing explicit transfer functions. Zhao et al. [59] optimized a control law consisting of two integrators and investigated the effects of structural parameters on the optimized DVA performance, see also [60,61] for addressing the possible force saturation problems. Besides, Meng et al. [62–64] designed delayed nonlinear DVAs and conducted optimization to reduce vibrations on nonlinear primary structures. Wang et al. [65] and Sun et al. [66–68] deployed electromagnetic shunt dampers to facilitate the realization of optimum parameters.

We note from the above that the existing research on H_∞ optimization to reduce resonance peaks seldom focuses on the antiresonance of the primary structure, and the effort aiming for an ideal zero antiresonance by tuning DR does not consider the adversely raised resonance peaks. To this end, this work proposes and addresses the H_∞ optimization problem of the DR to reduce the raised resonance peaks when achieving complete vibration suppression at the designated tuning frequency. One difficulty is due to the limited tunability of control parameters since the resonance of the DR for complete vibration suppression should be first guaranteed. Considering that H_∞ optimization is to reduce the effects of perturbations, which can be regarded as any excitation at a frequency different from the one where DR is tuned so it causes residual vibrations, we additionally incorporate feedback forces proportional to the nonzero responses of the primary structure into the total feedback forces for perturbation resistance. In this way, the total forces now stem from two aspects, one related to absorber states for the DR resonance as the classical cases, and the other (newly introduced) to the primary. Note that the feedback forces in the latter do not act at the tuning frequency where zero antiresonance is to be achieved, and thus such forces can suppress resonance peaks (nonzero vibrations) without affecting the tuning of the absorber-based feedback force for complete vibration suppression. Furthermore, given the known benefits of the delayed control, the newly introduced control term related to the primary structure is also delayed to seek further performance enhancement, finally yielding the so-called hybrid multiple-delayed DR (with both delayed states of the absorber and the primary structure). In addition to addressing the H_∞ optimization problem, we show that unduly reducing the resonance peaks can, however, significantly reduce the complete vibration suppression performance in terms of response speed and antiresonance band, and thus the trade-off between such two control tasks is also discussed to fully exploit the strength of the hybrid control logic. This work shows its novelty and offers its scientific contributions mainly in the following aspects:

- We propose and address the H_∞ optimization problem of the DR to limit the raised resonance peaks while achieving complete vibration suppression. For simplification, we design a hybrid multiple-delayed control law consisting of both delayed states of the absorber and the primary to reduce parametric coupling given that feedback forces based on the primary only affect nonzero responses thus unaffecting the tuning of the absorber-based force for DR resonance.
- An optimization framework is established. Particularly, system stability is addressed and the optimum shapes of the frequency response curves of the primary are investigated to simplify calculations. Furthermore, we discuss the trade-off between achieving lower resonance peaks and better complete vibration suppression performance so that significant performance enhancement can be simultaneously achieved in both aspects.

In what follows, Section 2 establishes system dynamics. Section 3 proposes the control law and the H_∞ optimization. Stability regions determining the bounds of optimum parameters are obtained in Section 4. Section 5 conducts constrained H_∞ optimization to balance the aforementioned trade-offs. Optimized parameters are shown in Section 6 and verified in Section 7. Section 8 draws conclusions. Italic symbols without a bar superscript '$\bar{\square}$' are dimensionless throughout the text.

2. Preliminaries

A common operating mode of the delayed resonator (DR) is shown in Fig. 1(a), where a force actuator $\bar{u}$ is injected into the vibration absorber to enhance the settling of the primary structure harmonically excited by $\bar{f}_e$. The stiffness and damping of the primary structure are denoted by $\bar{k}_p$ and $\bar{c}_p$, respectively. Similarly, we have $(\bar{k}_a, \bar{c}_a)$ for the absorber. Energy losses due to the friction between bearings and slides are modeled by linear dampers under good lubrication conditions with sufficient excitation [69], otherwise, see [20] for the effects of nonlinear frictions. Particularly, the damping related to the primary structure is incorporated into $\bar{c}_p$, and that related to the absorber is included by $\bar{c}_g$. The aim of DR is to completely settle the primary structure for $\bar{x}_p \equiv 0$ by properly tuning $\bar{u}$, as illustrated by Fig. 1(b). Upon achieving the aim, $(\bar{k}_p, \bar{c}_p)$ pose no effects to the primary except for balancing gravity due to $\bar{x}_p \equiv 0$, yielding the so-called complete vibration suppression. We next establish the basic system dynamics, review the tuning rules of the DR, and clarify the basis of the proposed hybrid control law.

2.1. Governing equations

Dynamics of the primary structure and the absorber in Fig. 1(a) are governed by

$$\begin{cases} \bar{m}_a\ddot{\bar{x}}_a + \bar{c}_g\dot{\bar{x}}_a + \bar{c}_a\left(\dot{\bar{x}}_a - \dot{\bar{x}}_p\right) + \bar{k}_a\left(\bar{x}_a - \bar{x}_p\right) = \bar{u}, \\ \bar{m}_p\ddot{\bar{x}}_p + \bar{c}_p\dot{\bar{x}}_p + \bar{k}_p\bar{x}_p + \bar{c}_a\left(\dot{\bar{x}}_a - \dot{\bar{x}}_a\right) + \bar{k}_a\left(\bar{x}_p - \bar{x}_a\right) = \bar{f}_e - \bar{u}, \end{cases} \tag{1}$$

where $\bar{m}_a$ and $\bar{m}_p$ denote the masses of the primary structure and the absorber, respectively; $\bar{x}_p$ and $\bar{x}_a$ the absolute displacements; $\bar{x}_{(\cdot)}$, $\bar{u}$, and $\bar{f}_e$ are all functions of the time $\bar{t}$. Performing the following transformations

$$\begin{gathered} \bar{\omega}_p = \sqrt{\bar{k}_p/\bar{m}_p}, \bar{\omega}_a = \sqrt{\bar{k}_a/\bar{m}_a}, \zeta_p = \frac{\bar{c}_p}{2\bar{m}_p\bar{\omega}_p}, \zeta_a = \frac{\bar{c}_a}{2\bar{m}_a\bar{\omega}_a}, \zeta_g = \frac{\bar{c}_g}{2\bar{m}_a\bar{\omega}_a}, \\ \mu = \frac{\bar{m}_a}{\bar{m}_p}, v = \frac{\bar{\omega}_a}{\bar{\omega}_p}, x_a = \frac{\bar{x}_a}{\bar{l}}, x_p = \frac{\bar{x}_p}{\bar{l}}, t = \bar{t}\bar{\omega}_p, f_e = \frac{\bar{f}_e}{\bar{k}_p\bar{l}}, u = \frac{\bar{u}}{\bar{k}_p\bar{l}}, \end{gathered} \tag{2}$$

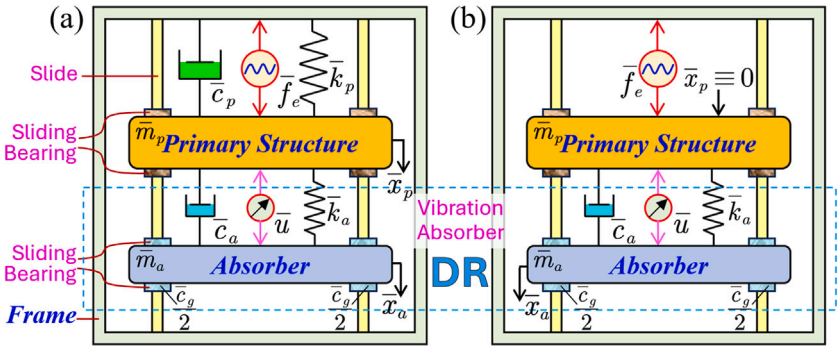

Fig. 1. The system to be handled. (a). An operating mode of DR for settling a force-excited primary structure. (b). Reduced model of (a) when the primary structure is completely settled.

in which $\bar{l}$ denotes the unit length, yields the dimensionless governing equations

$$\begin{cases} \mu\left[\ddot{x}_a + 2\zeta_g \upsilon \dot{x}_a + 2\zeta_a \upsilon\left(\dot{x}_a - \dot{x}_p\right) + \upsilon^2\left(x_a - x_p\right)\right] = u, \\ \ddot{x}_p + 2\zeta_p \dot{x}_p + x_p + \mu\left[2\zeta_a \upsilon\left(\dot{x}_p - \dot{x}_a\right) + \upsilon^2\left(x_p - x_a\right)\right] = f_e - u. \end{cases} \tag{3}$$

By tuning the feedback actuation force u, the desired complete vibration suppression aims for $x_p \equiv 0$ when $f_e \neq 0$.

2.2. Tuning rules of the DR for $x_p \equiv 0$

The goal is to seek the condition for u to render Eq. (3) a fixed solution $x_p \equiv 0$. Letting $x_p \equiv 0$, Eq. (3) reduces to

$$\begin{cases} \mu\left(\ddot{x}_a + 2\left(\zeta_a + \zeta_g\right)\upsilon \dot{x}_a + \upsilon^2 x_a\right) = u, \\ -\mu\left(2\zeta_a \upsilon \dot{x}_a + \upsilon^2 x_a\right) = f_e - u, \end{cases} \quad or \quad \begin{cases} \bar{m}_a \ddot{\bar{x}}_a + \bar{c}_g \dot{\bar{x}}_a + \bar{c}_a \dot{\bar{x}}_a + \bar{k}_a \bar{x}_a = \bar{u}, \\ -\left(\bar{c}_a \dot{\bar{x}}_a + \bar{k}_a \bar{x}_a\right) = \bar{f}_e - \bar{u}, \end{cases} \tag{4}$$

in which the first equation corresponds to the reduced absorber dynamics in Fig. 1(b), and the other one signifies that all forces exerted on the primary structure are naturalized, an obvious prerequisite for $x_p \equiv 0$. From the first equation in (4), the control law for u to achieve $x_p \equiv 0$ must (partially) depend on absorber states. Applying the Laplace transform, we have

$$\mu\left(s^2 + 2\left(\zeta_a + \zeta_g\right)\upsilon s + \upsilon^2\right) X_a = U_a(s)\, X_a, \tag{5}$$

where s is the Laplace variable, $X_a = \mathscr{L}\left(x_a\right)$, with the notation $\mathscr{L}(\cdot)$ denoting the Laplace transform operation, and U_a is the transfer function from the absorber states to the feedback force u in steady states $x_p \equiv 0$. Denoting the actual excitation frequency as $\bar{\omega} \in \mathbb{R}^+$, both x_a and u in steady states should be at the associated dimensionless frequency $\omega = \bar{\omega}/\bar{\omega}_p$ as per the second equation in (4). Substituting $s = j\omega$, $j = \sqrt{-1}$ into (5) and separating the real and imaginary parts lead to

$$\begin{cases} \mathrm{Re}\left(U_a(s = j\omega)\right) = \upsilon^2 - \omega^2, \\ \mathrm{Im}\left(U_a(s = j\omega)\right) = 2\left(\zeta_a + \zeta_g\right)\upsilon\omega, \end{cases} \tag{6}$$

which is the necessary condition for tuning u to achieve $x_p \equiv 0$, regardless of the forms of the control logic for u. Following the DR prototype [4], the absorber displacement-based control logic is considered for comparison,

$$u_a(t, g, \tau) = g x_a\left(t - \tau_a\right), \tag{7}$$

where g is the feedback gain and $\tau_a \geqslant t_{loop}$ is the time delay, two dimensionless control parameters, with t_{loop} denoting the inevitable loop delay. By introducing the delay τ_a as a control parameter, a single control term is of two manipulable parameters, thus enhancing the control robustness, in addition to taking into account the loop delay for achieving vibration suppression in a 'complete' manner [25].

Substituting (7) into (6), i.e., $U_a(s) = g e^{-\tau_a s}$, yields the tuned pair of $\left(g, \tau_a\right)$ as

$$\begin{cases} g_t\left(\omega_t\right) = \pm\mu\sqrt{\left(\upsilon^2 - \omega_t^2\right)^2 + 4\upsilon^2\omega_t^2\left(\zeta_a + \zeta_g\right)^2}, \\ \tau_{a,t}\left(\omega_t\right) = \frac{1}{\omega_t}\left[\mathrm{a\tan}\left(\frac{-2\left(\zeta_a + \zeta_g\right)\upsilon\omega_t}{\upsilon^2 - \omega_t^2}\right) + 2\pi\left(b - 1\right) + \rho\pi\right], \end{cases} \tag{8}$$

where the subscript $(\cdot)_t$ denotes 'tuned'; ω_t is the tuning frequency stemming from the detection of the excitation frequency ω; $\rho = 0$ when $g_t > 0$, and $\rho = 1$ when $g_t < 0$; $b \in \mathbb{Z}^+$ stemming from the periodicity of the $\tan(\cdot)$ function is called branch number, see [4] for explaining the mechanism of different b based on the root loci of (5). Note that $\left(g_t, \tau_{a,t}\right)$ are both optional at a given tuning frequency ω_t and that the complete vibration suppression necessitates that $\omega_t = \omega$.

Remark 1. The delay parameter τ_a should be corrected as $\tau_a - t_{loop}$ in practice to exclude the loop delay [23]. However, this correction is not considered in the text to reduce distraction. Alternatively, we take it as a default operation of the controller. ■

2.3. Frequency response function with a general form of u

The DR tuned with $\left(g_t, \tau_{a,t}\right)$ is effective in suppressing single-frequency vibrations. Residual vibrations $\left|x_p\right| \neq 0$ appear when frequency mismatch $\omega_t \neq \omega$ occurs. To reduce such residual vibrations, we generalize the control law of u by additionally considering the states of the primary structure

$$u(t) = u_a(t) + u_p(t), \tag{9}$$

which is the general form of the linear superposition of control terms related to the linear states of the absorber (u_a) and the primary structure (u_p). The Laplace transform of the control law (9) is

$$U(s) = U_a(s)\, X_a + U_p(s)\, X_p, \tag{10}$$

where $X_p = \mathscr{L}\left(x_p\right)$, and U_p is the transfer function from x_p to u_p. Substituting (9) into (3), system dynamics in the Laplace domain can be written in a matrix form of

$$\mathbf{Z}\left(s, U_a, U_p\right)\mathbf{X} = \mathbf{F}, \tag{11}$$

where $\mathbf{X} = \left[X_a, X_p\right]^{\mathrm{T}}$, $\mathbf{F} = \left[0, F_e\right]^{\mathrm{T}}$, $F_e = \mathscr{L}\left(f_e\right)$, and

$$\mathbf{Z}\left(s, U_a, U_p\right) = \begin{bmatrix} z_{11}(s) & z_{12}(s) \\ z_{21}(s) & z_{22}(s) \end{bmatrix}, \tag{12}$$

in which

$$\begin{cases} z_{11}(s) = \mu\left(s^2 + 2\left(\zeta_a + \zeta_g\right)\upsilon s + \upsilon^2\right) - U_a(s), \\ z_{12}(s) = -\mu\upsilon\left(2\zeta_a s + \upsilon\right) - U_p(s), \\ z_{13}(s) = -\mu\upsilon\left(2\zeta_a s + \upsilon\right) + U_a(s), \\ z_{22}(s) = s^2 + 2\zeta_p s + 1 + \mu\upsilon\left(2\zeta_a s + \upsilon\right) + U_p(s). \end{cases} \tag{13}$$

We can then obtain the transfer function from f_e to x_p by calculating the $(2,2)$ element of $\mathbf{Z}^{-1}$

$$G\left(s,U_a,U_p\right)=\frac{X_p}{F_e}=\mathbf{Z}^{-1}_{(2,2)}=\frac{\mu\left(s^2+2\left(\zeta_a+\zeta_g\right)\upsilon s+\upsilon^2\right)-U_a\left(s\right)}{\left|\mathbf{Z}\left(s,U_a,U_p\right)\right|}, \tag{14}$$

leading to the frequency response function of the primary structure

$$\left|x_p\left(\omega\right)\right|=\frac{\left|\bar{f}_e\right|}{\bar{k}_p\bar{l}}A\left(\omega\right),A\left(\omega\right)=\left|G\left(s=j\omega\right)\right|. \tag{15}$$

Note that the numerator of (14) concurs with (5) and is independent of U_p, and thus u_p does not affect the tuning mechanism of u_a for complete vibration suppression, agreeing with (6). The characteristic equation concurs with the denominator of (14),

$$CE\left(s,U_a,U_p\right)=\left|\mathbf{Z}\left(s,U_a,U_p\right)\right|=0, \tag{16}$$

the root spectrum of which must lie within the left half of the complex plane for stability. Remarkably, U_p appears in (16), and thus the control force u_p affects system stability and the residual vibrations signified by $\left|x_p\right|\neq 0$ in light of (15). Hence, properly designing u_p can possibly enhance vibration suppression without affecting the tuning of u_a, i.e., Eq. (6).

3. Hybrid multiple-delayed control law and optimization problem

A tuned DR achieves complete vibration suppression by creating a zero antiresonance of x_p at ω_t as per (15) but compromises the raised resonance peaks. We next show such adverse effects and how they can be reduced by designing u_p.

3.1. Hybrid multiple-delayed control law

To exploit the benefits of u_p in light of (14), we revamp the classical DR scheme (7) by additionally including the displacement x_p of the primary structure into the feedback loop, yielding a hybrid control law with both states of x_a and x_p,

$$u_{ap}\left(t\right)=g\left[x_a\left(t-\tau_a\right)+\beta x_p\left(t-\tau_p\right)\right], \tag{17}$$

where β is the gain and τ_p is an additional delay to seek possible additional benefits without increasing the number of control terms similar to τ_a, thus creating the so-called hybrid multiple-delayed control law. We point out this control law is inspired by [38], where, however, different objectives for a different system are considered. For (17), the control parameter composition $\left(g,\tau_a,\beta,\tau_p\right)$ denoted as $\mathbf{\Theta}$ is meaningful when the system is stable, and we define

$$\mathbf{\Theta}_{stable}=\left\{\mathbf{\Theta}\left|\begin{array}{l}\max\left(\mathrm{Re}\left(s\right)\right)<0,\\ s\in\Sigma\left(CE\left(s,\mathbf{\Theta}\right)=0\right).\end{array}\right.\right\}, \tag{18}$$

where $\Sigma\left(\cdot\right)$ denotes calculating the characteristic spectrum. Substituting u_{ap} into (15) following Eqs. (9)–(14) leads to

$$A\left(\omega,g,\tau_a,\beta,\tau_p\right)=\left|\frac{\mu\left(s^2+2\left(\zeta_a+\zeta_g\right)\upsilon s+\upsilon^2\right)-U_a\left(s,g,\tau_a\right)}{\left|\mathbf{Z}\left(s,U_a\left(s,g,\tau_a\right),U_p\left(s,g,\beta,\tau_p\right)\right)\right|}\right|_{s=j\omega}, \tag{19}$$

which is called amplitude magnification factor (AMF), where $U_a=ge^{-\tau_a s}$ and $U_p=g\beta e^{-\tau_p s}$. For discrimination, the DR actuated with u_a in (7) and u_{ap} in (17) is called A-DR and AP-DR, respectively.

Note that the AP-DR is reduced to A-DR when $\beta=0$, and the tuning rules of $\left(g_t,\tau_{a,t}\right)$ in (8) for complete vibration suppression apply to both the A-DR and the AP-DR, regardless of the values of $\left(\beta,\tau_p\right)$. The independence of the tuned pair $\left(g_t,\tau_{a,t}\right)$ from $\left(\beta,\tau_p\right)$ or u_p significantly simplifies the optimization of $\left(\beta,\tau_p\right)$ to reduce residual vibrations $\left|x_p\right|\neq 0$. In addition, $u_p\equiv 0$ when $\left|x_p\right|=0$.

Remark 2. Compared with classical DRs which are mainly driven by purely absorber-based control laws, the restriction of the hybrid multiple-delayed control law (17) can be the need for additional sensors to get the states of the primary. However, this should not be a problem in practice since in the cases where active control is required, the primary is usually real-time monitored to determine whether active control should be deployed or whether emergency actions to ensure safety should be activated. ■

3.2. Frequency response analysis

To test the complete vibration suppression performance, we consider a coupled system governed by

$$\begin{aligned}&\mu=0.5285,\upsilon=0.9862,\zeta_a=0.1097,\zeta_g=0.051,\zeta_p=0.0665,\\&\bar{\omega}_p=38.96\ \mathrm{rad/s}\left(6.20\ \mathrm{Hz}\right),\bar{\omega}_a=38.42\ \mathrm{rad/s}\left(6.11\ \mathrm{Hz}\right),\end{aligned} \tag{20}$$

and the corresponding experimental setup is to be introduced in Section 7.1. Variations of the tuned pairs $\left(g_t,\tau_{a,t}\right)$ at the branch $\left(g_t<0,b=1\right)$ with respect to the tuning frequency following $\bar{\omega}_t=\omega_t\bar{\omega}_p$ are shown in Fig. 2(a), where the minimum tuned gain amplitude $\left|g_t\right|$ appears around the natural frequency $\bar{\omega}_a$ of the absorber, signifying that smaller feedback actuation forces u are needed here to alter the passive absorber dynamics for complete vibration suppression, consistent with the practice.

Let us further examine four specific tuning frequencies $\bar{\omega}_t=[5,6,7,8]$ Hz. Accordingly, the spectra of the characteristic Eq. (16) calculated by the QPmR algorithm [70] and the AMF $A\left(\omega\right)$ as per (19) with respect to various control parameter compositions $\mathbf{\Theta}$ are shown in Fig. 2(b–d). From Fig. 2(b), a tuned A-DR ($\beta=0$) does not necessarily lead to complete vibration suppression since the system can lose stability, as exemplified by the case $\bar{\omega}_t=5$ Hz. On the other hand, Fig. 2(c) shows that a passive absorber yields nonideal antiresonance around $\bar{\omega}_a$, and the tuned A-DR achieves ideal zero antiresonance at the tuning frequency independent of $\bar{\omega}_a$. However, achieving zero antiresonance by the A-DR significantly raises the resonance peaks. Compared with the passive case, the resonance peak can be raised by more than 930% (from 3.43 to 35.4 for $\bar{\omega}_t=6$ Hz). Consequently, while achieving effective vibration suppression at the tuning frequency ω_t using the A-DR, an additional perturbation force at the resonance frequency may cause significant vibrations, leading to high risks of structural failures even if the perturbation force is temporary and small. Note that such perturbation forces can also be explained as the excitation force f_e if $\omega\neq\omega_t$. In such cases, the tuned A-DR amplifies vibrations thus acting contradictorily to its original design purpose. Solutions reflected in Fig. 2(d) related to the AP-DR case are discussed later in Section 3.4.

3.3. Optimization problem (theoretical): Minimizing resonance peaks by tuning $\left(\beta,\tau_p\right)$

The aim is now to minimize the highest resonance peak of the primary structure when $\left(g,\tau_a\right)=\left(g_t,\tau_{a,t}\right)$ to limit the maximum vibration amplitude caused by the frequency mismatch $\omega_t\neq\omega$. From Eq. (15), we have

$$\left|x_p\left(\omega\right)\right|\leqslant h\left(g,\tau_a,\beta,\tau_p\right)\times\left|f_e\right|_{\max} \tag{21}$$

for the proposed AP-DR actuated with the proposed hybrid multiple-delayed control logic u_{ap} in (17), where $\left|f_e\right|_{\max}$ denotes the maximum amplitude of the dimensionless excitation force exerted on the primary structure, and

$$\begin{aligned}h\left(g,\tau_a,\beta,\tau_p\right)&=\left\|A\left(\omega,g,\tau_a,\beta,\tau_p\right)\right\|_\infty\\&=\max\left\{A\left(\omega,g,\tau_a,\beta,\tau_p\right)\right\}.\end{aligned} \tag{22}$$

Note that h is independent of ω. Then, the task is to minimize the H_∞ norm h, yielding the so-called H_∞ optimization that is widely adopted

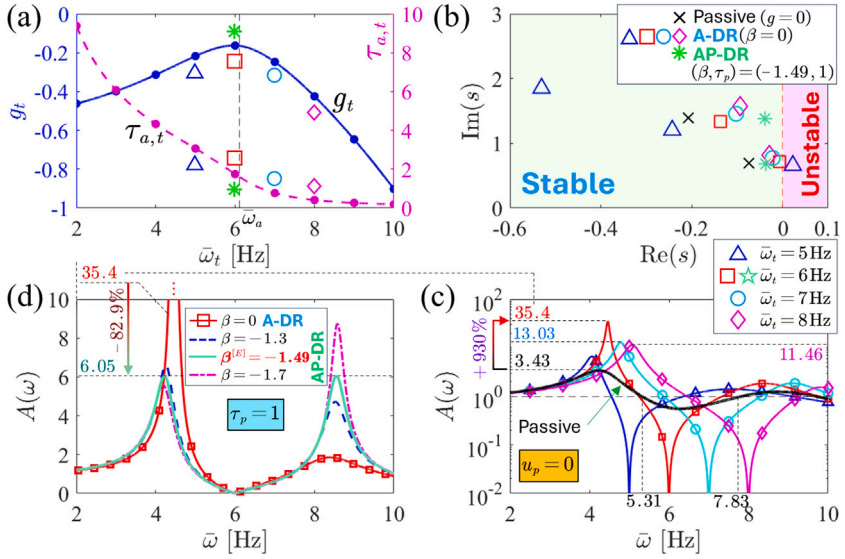

Fig. 2. Demonstration of the raised resonance peaks when the tuned A-DR achieves complete vibration suppression and the effects of the AP-DR on manipulating frequency responses for the system (20). (a). Variations of tuned pairs $(g_t, \tau_{a,t})$ for $(g_t < 0, b = 1)$ with respect to $\bar{\omega}_t$. (b). Spectral variations of the characteristic Eq. (16) for various control parameter compositions $\boldsymbol{\Theta}$. (c). Variations of frequency responses following the AMF $A(\omega)$ in (15) in the A-DR and passive cases. (d). Variations of $A(\omega)$ in the cases of A-DR and AP-DR with $\tau_p = 1$. Abscissas in (c, d) are scaled as $\bar{\omega} = \omega/\bar{\omega}_p$.

for designing passive absorbers to enhance (incomplete) vibration reduction, as aforementioned.

To simultaneously fulfill the two tasks of H_∞ optimization and the complete vibration suppression, the classical A-DR is inoperable since its two manipulable control parameters (g, τ_a) are always tuned as per (8) for the latter task, see also Fig. 2(c). Alternatively, the additional feedback force u_p by adopting the AP-DR provides two independent control parameters (β, τ_p) to additionally achieve the H_∞ optimization, leading to the optimization rule of (β, τ_p) as

$$\left(\beta_{opt}, \tau_{p,opt}\right)_{[\omega_t]} = \left\{ (\beta, \tau_p) \left\{ \begin{array}{l} \min\limits_{(\beta,\tau_p)} \left\{ h\left(g_t(\omega_t), \tau_{a,t}(\omega_t), \beta, \tau_p\right) \right\}, \\ s.t.: \left(g_t(\omega_t), \tau_{a,t}(\omega_t), \beta, \tau_p\right) \in \boldsymbol{\Theta}_{stable}. \end{array} \right. \right\}, \tag{23}$$

a min–max problem subject to the stability condition (18), where the subscript $[\omega_t]$ highlights that $(g, \tau_a) = (g_t(\omega_t), \tau_{a,t}(\omega_t))$, i.e., optimizing (β, τ_p) to minimize h should not affect the complete vibration suppression at the tuning frequency ω_t. We here remark that Eq. (23) only subject to stability constraint is valid for an ideal system for theoretical analysis, and issues in practical applications are investigated in Section 5, where additional constraint conditions are complemented.

3.4. Equal-peak feature

Fig. 2(d) previews the benefits of tuning (β, τ_p) in reducing h in the case $\bar{\omega}_t = 6$ Hz. One can find that for a given delay τ_p, a critical value of β, i.e., $\beta^{[E]} = -1.49$ when $\tau_p = 1$, exists so that two different resonance peaks are equal. Once β deviates from $\beta^{[E]}$, either of such two peaks raises, making a minimum of h appears when $\beta = \beta^{[E]}$. The feature that such a minimum $h_{\min} = 6.05$ appears at the critical moment when different resonance peaks are at the same height makes the H_∞ optimization also widely called equal-peak optimization [51,62,63]. Besides, the system is stable when $(\beta, \tau_p) = (-1.49, 1)$ as per Fig. 2(b), and thus the highest resonance peak in the classical A-DR case is significantly reduced by 82.9% by adopting an AP-DR optimized with $(\beta, \tau_p) = (\beta^{[E]}, 1)$, as marked in Fig. 2(d). Note that $\beta^{[E]}$ and $h_{\min}$ here are local optima since τ_p is fixed. The equal-peak feature provides a critical analytical condition to simplify optimization calculations, while it is not a necessary condition to perform the H_∞ optimization for the considered AP-DR, as to be further investigated in Section 5.

Remark 3. In the passive case, if the absorber has a heavy ground damping ζ_g, $h_{\min}$ can appear when $A(\omega)$ only has a single resonance peak [71]. However, this reduced case does not exist here since the tuned pair $(g_t, \tau_{a,t})$ always creates a zero antiresonance at ω_t, i.e., $A(\omega_t, g_t, \tau_{a,t}) = 0$ regardless of (β, τ_p), see Fig. 2(c, d). Besides, since one goal of tuning $(g_t, \tau_{a,t})$ is to neutralize the absorber damping effect at ω_t as per (6), smaller values (c_a, c_p) are adopted, which also lowers energy consumption [7]. Hence, at least two resonance peaks separately appear on the two sides of the tuning frequency ω_t. ■

4. Stable regions of (β, τ_p)

Before formally handling the optimization (23), the constraint condition related to system stability (18) can be simplified by explicitly determining the stable regions of (β, τ_p) for a given pair of $(g_t, \tau_{a,t})$. The knowledge of such stable regions determines the operable search interval of $(\beta_{opt}, \tau_{p,opt})$ without needing the numerical spectral checks as in Fig. 2(b).

4.1. Stability boundaries

Stability losses of linear systems must occur at the critical moment when the characteristic equation exhibits at least one pair of imaginary roots. To this end, substituting the Laplace transform of (17) and $s = j\omega_c, \omega_c \in 0 \cup \mathbb{R}^+$ into (16) yields

$$CE\left(j\omega_c, \beta_c, \tau_{p,c}\right) = \left| \mathbf{Z}\left(s = j\omega_c, U_a = g_t e^{-j\tau_{a,t}\omega_c}, U_p = g_t \beta_c e^{-j\tau_{p,c}\omega_c}\right) \right| = 0, \tag{24}$$

where the subscript $(\cdot)_c$ denotes 'critical'. Clearly, the exhaustive solution pairs $(\beta_c, \tau_{p,c})$ of (24) signify the critical moments of destabilization and thus are called stability boundaries. To solve Eq. (24), we start with separating U_p in (16), yielding

$$\beta_c e^{-\tau_{p,c} s} = \frac{\sum_{i=0}^{4} \varphi_i\left(g_t, \tau_{a,t}\right) s^i}{g_t\left(\mu s\left(2\upsilon\zeta_g\right) + s\right)}, \tag{25}$$

where φ_i denote real coefficients in $(g_t, \tau_{a,t})$. Substituting $s = j\omega_c$ into (25) and separating the real and imaginary parts on both sides of this equation leads to

$$\beta_c\left(\cos\left(\tau_{p,c}\omega_c\right) - j\sin\left(\tau_{p,c}\omega_c\right)\right) = \sigma\left(\omega_c, g_t, \tau_{a,t}\right) + j\varpi\left(\omega_c, g_t, \tau_{a,t}\right), \tag{26}$$

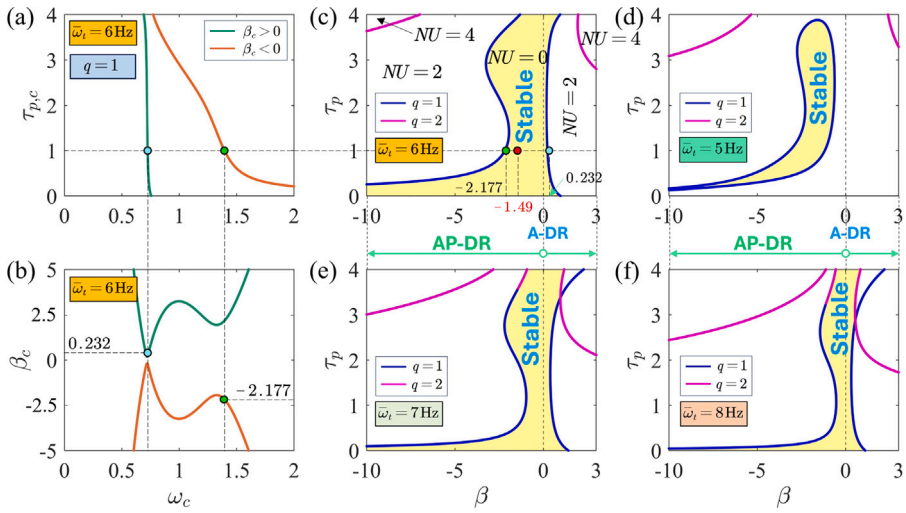

Fig. 3. Stability analysis based on stability boundaries $(\beta_c, \tau_{p,c})$ for the system (20). (a, b). Variations of $(\beta_c, \tau_{p,c})$ versus ω_c for $\bar{\omega}_t = 6$ Hz and $q = 1$. (c–f). Stability maps on the (β, τ_p) plane for $\bar{\omega}_t \in [5, 6, 7, 8]$ Hz, where colored regions are stable. In all cases, $(g_t, \tau_{a,t})$ are tuned with $(g_t < 0, b = 1)$ following Fig. 2(a), and 'NU' denotes the number of unstable roots.

where $(\sigma, \varpi) \in \mathbb{R}^2$ are parameterized in $(\omega_c, g_t, \tau_{a,t})$ and stem from the right-side term of (25). Balancing the real and imaginary parts of Eq. (26), $(\beta_c, \tau_{p,c})$ can be obtained in closed forms as

$$\begin{cases} \beta_c(\omega_c) = \pm\sqrt{\sigma^2(\omega_c, g_t, \tau_{a,t}) + \varpi^2(\omega_c, g_t, \tau_{a,t})}, \\ \tau_{p,c}(\omega_c) = \frac{1}{\omega_c}\left[\operatorname{atan}\left(\frac{-\varpi(\omega_c, g_t, \tau_{a,t})}{\sigma(\omega_c, g_t, \tau_{a,t})}\right) + 2\pi(q-1) + \rho_c\pi\right], \end{cases} \tag{27}$$

where $\rho_c = 0$ when $\beta_c > 0$, $\rho_c = 1$ when $\beta_c < 0$, and $q \in \mathbb{Z}^+$ stems from the periodicity of the $\tan(\cdot)$ function similar to the branch number b of the tuned delay $\tau_{a,t}$ in (8). Note that one ω_c corresponds to two β_c at most and infinitely many critical delays $\tau_{p,c}$ due to the effects of q. By sweeping $\omega_c \in \mathbb{R}^+$, the stability boundaries $(\beta_c, \tau_{p,c})$ can be obtained.

4.2. Stability map

Taking $\bar{\omega}_t = 6$ Hz and $(g_t < 0, b = 1)$ as an example, i.e., $(g_t, \tau_{a,t}) = (-0.1633, 1.7455)$ as per Fig. 2(a), variations of $(\beta_c, \tau_{p,c})$ with $q = 1$ are shown in Fig. 3(a, b). From Fig. 3(b), at most two solutions of β_c exist for a given ω_c, and such two solutions are opposite to each other, agreeing with the form of Eq. (27). Combining Fig. 3(a) and (b), the relationship between β_c and $\tau_{p,c}$ on the (β, τ_p) plane constitutes stability boundaries, as shown in Fig. 3(c).

Each point $(\beta_c, \tau_{p,c})$ on the stability boundaries in Fig. 3(c) corresponds to at least one pair of imaginary roots $s = \pm j\omega_c$ of the characteristic Eq. (16). Particularly, such stability boundaries are continuous and divide the (β, τ_p) plane into infinitely many pockets. Variations of (β, τ_p) within each pocket do not alter the stability of this pocket since destabilization requires that the rightmost characteristic roots shift from the left half of the complex plane to the right [72]. To this end, we numerically check the stability of one pocket by counting the number of unstable roots (NU) related to one point within this pocket as in Fig. 2(b). For the stability of rest pockets, we count NU based on the number of boundary crossings from the checked pocket with

$$RT = \operatorname{sgn}\left[\operatorname{Re}\left(\frac{ds}{d\lambda}\bigg|_{\substack{s=j\omega_c \\ \lambda=\lambda_c}}\right)\right], \tag{28}$$

which is known as the root tendency [73], where $\lambda \in [\beta, \tau_p]$ signifies the variable that crosses the stability boundaries $(\beta_c, \tau_{p,c})$. Clearly, a crossing with $RT = +1$ and $RT = -1$ increases and decreases NU, respectively. The resulting distributions of NU at each pocket for $\bar{\omega}_t = 6$ Hz are marked in Fig. 3(c), where the stable regions corresponding to $NU = 0$ are colored.

4.3. Comparisons

Following the analysis procedure in Fig. 3(c), the stable regions of (β, τ_p) for $\bar{\omega}_t = [5, 7, 8]$ Hz are colored in Fig. 3(d, e, f) for comparisons. Revisiting the numerical spectral checks in Fig. 2(b), the system in the A-DR case when $\bar{\omega}_t = 5$ Hz is unstable. Such instability is also reflected in Fig. 3(d), where $\beta = 0$ lies outside the stable region. Note also that such instability can be recovered by adopting an AP-DR, signifying another benefit of AP-DR to extend the operable low-frequency band of complete vibration suppression in addition to reducing the resonance peak h of the primary structure, as to be further verified in Section 7. Besides, Fig. 3(e) and (f) show that the A-DR is stable when $\bar{\omega}_t = [7, 8]$ Hz, which also agrees with Fig. 2(b).

On the other hand, for optimizing the AP-DR with $\tau_p = 1$ when $\bar{\omega}_t = 6$ Hz, as previously considered in Fig. 2(d), the search interval for the optimum of β to reduce resonance peaks can now be limited to $\beta \in [-2.168, 0.232]$ as per Fig. 3(c). Clearly, $\beta^{[E]} = -1.49$ obtained in Fig. 2(d) to achieve the equal-peak feature lies within the stable region, and thus the system is stable, again agreeing with the spectral check in Fig. 2(b). Hence, with the stability maps as Fig. 3(b–e), the constraint condition in (23) for system stability (18) can be guaranteed by limiting the search interval of $(\beta_{opt}, \tau_{p,opt})$ within stable regions.

At last, one can find that the stable regions of (β, τ_p) are broader when $\beta < 0$. A direct reason is that $\beta g_t > 0$ holds in this case so that the feedback forces related to u_p tend to settle the primary structure. For comparisons, Fig. 4 shows the cases where $(g_t, \tau_{a,t})$ are tuned with $(g_t > 0, b = 1)$. In this case, stable regions of (β, τ_p) now tend to appear when $\beta > 0$.

5. H_∞ optimization of the AP-DR

Having obtained the stable regions of (β, τ_p), we next handle the optimization problem (23) to minimize the resonance peak h at a given tuning frequency ω_t. The analysis starts with investigating the issues with this problem based on an intuitive numerical case. Then, additional constraint conditions are complemented for remedies, with analytical conditions established to simplify calculations. When tuning $(g_t, \tau_{a,t})$, the branch $(g_t < 0, b = 1)$ is always considered without loss of generality.

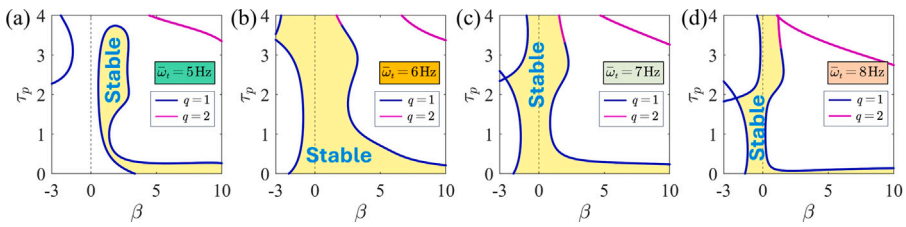

Fig. 4. Stability maps on the (β, τ_p) plane for the system (20) when $(g_t, \tau_{a,t})$ are tuned with $(g_t > 0, b = 1)$ for different tuning frequencies $\bar{\omega}_t$ as per Fig. 2(a). Colored regions are stable, which are obtained following the analysis procedure in Fig. 3. (a). $\bar{\omega}_t = 5$ Hz. (b). $\bar{\omega}_t = 6$ Hz. (c). $\bar{\omega}_t = 7$ Hz. (d). $\bar{\omega}_t = 8$ Hz.

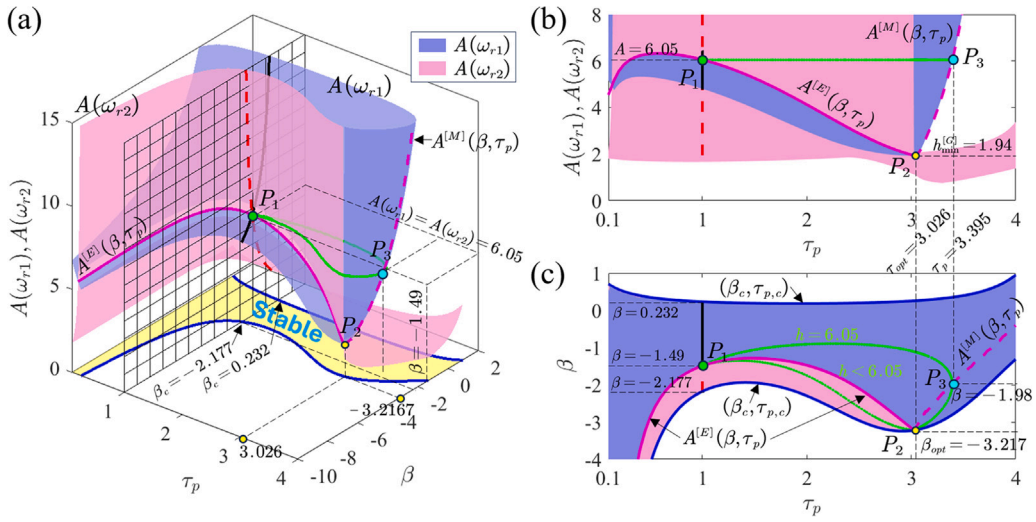

Fig. 5. Variations of the first two highest resonance peaks $(A(\omega_{r1}), A(\omega_{r2}))$ with respect to (β, τ_p) when $\bar{\omega}_t = 6$ Hz for the coupled system (20). Only (β, τ_p) pairs rendering system stable are considered. (a). 3D view. (b, c). 2D projection. Solid curve $A^{[E]}(\beta, \tau_p)$: Intersection of surfaces $A(\omega_{r1})$ and $A(\omega_{r2})$. Dashed curve $A^{[M]}(\beta, \tau_p)$: Minima of h without intersection.

5.1. Optimization based on numerical sweeping and issues in practical applications

We define ω_{r1} and ω_{r2}, $\omega_{r1} < \omega_{r2}$, as the frequencies of the first two highest resonance peaks of $A(\omega)$. For $\bar{\omega}_t = 6$ Hz, we sweep (β, τ_p) within the stable region obtained in Fig. 3(c). Fig. 5 shows the resulting variations of $(A(\omega_{r1}), A(\omega_{r2}))$.

The equal-peak feature-based optimization to reduce the resonance peak h can be intuitively found in Fig. 5(a), where the grids denote the case $\tau_p = 1$ previously considered in Fig. 2(d). As β increases from $\beta = -2.177$ when $\tau_p = 1$, $A(\omega_{r2})$ reduces and $A(\omega_{r1})$ increases. The critical moment $A(\omega_{r1}) = A(\omega_{r2}) = 6.05$ when $\beta = -1.49$ yields a minimum of h, i.e., point P_1, agreeing with Fig. 2(d). Clearly, the intersection curve of the two surfaces $A(\omega_{r1})$ and $A(\omega_{r2})$ corresponds to the equal-peak feature, and we use the notation $A^{[E]}(\beta, \tau_p)$ to denote the amplitude variations of the intersection curve with respect to (β, τ_p). Note that $A^{[E]}(\beta, \tau_p)$ if exists for a given τ_p always corresponds to a minimum of h as β varies.

From Fig. 5(b), the aforementioned intersection point P_1 for $A^{[E]} = 6.05$ only corresponds to a local minimum of h, and the global minimum can be found as $h_{\min}^{[G]} = 1.94$, which also appears on the curve $A^{[E]}(\beta, \tau_p)$, i.e., point P_2. Accordingly, we can obtain the optimum pair $(\beta_{opt}, \tau_{p,opt}) = (-3.217, 3.026)$ as per Fig. 5(c). We stress that although the curve $A^{[E]}(\beta, \tau_p)$ is truncated by stability boundaries $(\beta_c, \tau_{p,c})$, one has $(\beta_{opt}, \tau_{p,opt}) \neq (\beta_c, \tau_{p,c})$, otherwise $A(\omega_c, \beta_{opt}, \tau_{p,opt}) \to \infty$ and the system is marginally stable, see the forms of (19) and (24). Consequently, determining $(\beta_{opt}, \tau_{p,opt})$ by directly sweeping $(\beta_c, \tau_{p,c})$ is inoperable. Note also that the analytical expression of the curve $A^{[E]}(\beta, \tau_p)$ is unclear. Next, the AMF $A(\omega)$ associated with the obtained $(\beta_{opt}, \tau_{p,opt})$, the passive case ($g = 0$), and the A-DR case ($\beta = 0$) are compared in Fig. 6(a).

The equal-peak feature of the resonance peaks resulting from the AP-DR optimized with $(\beta_{opt}, \tau_{p,opt})$ can be clearly found in Fig. 6(a). Compared with the A-DR, the AP-DR reduces the resonance peak h by up to 94.5%, making $h_{\min}^{[G]}$ even smaller than h in the passive case. However, such a significant reduction of h compromises the capacity of complete vibration suppression. Compared with the A-DR, a small mismatch between ω_t and the excitation frequency ω in the AP-DR case with $(\beta_{opt}, \tau_{p,opt})$ leads to significant residual vibrations that can even be more dominant than those in the passive case, thus jeopardizing complete vibration suppression in practice. Besides, from the spectral distributions in Fig. 6(b), the dominant (i.e., rightmost) root s_{dom} related to $(\beta_{opt}, \tau_{p,opt})$ is very close to the imaginary axis, and thus the duration for settling the primary structure can be undesirably long. Based on the above, achieving the global minimum $h_{\min}^{[G]}$ may not be the best choice.

To facilitate the realization of complete vibration suppression, we now do not pursue the maximum reduction of h. Let us reconsider the previous case $\tau_p = 1$, where the unique local minimum now denoted as $h_{\min}^{[L]} = 6.05$ appears at $\beta = -1.49$. The corresponding AMF is also shown in Fig. 6(c) and is zoomed in Fig. 6(d). In this case, the resonance peak in the A-DR case is significantly reduced while extending the antiresonance valley at ω_t. Besides, from Fig. 6(b), s_{dom} in the AP-DR case lies further on the left half of the complex plane than that in the A-DR case, signifying a favorably shorter settling time.

On the other hand, we remark that the equal-peak feature is not a necessary condition to reduce h in the A-DR case. In Fig. 5, the dashed curve marked as $A^{[M]}(\beta, \tau_p)$ denotes the local minima $h_{\min}^{[L]}$ when the equal-peak feature does not exist. An alternative solution for $h = 6.05$ can be $(\beta, \tau_p) = (-1.98, 3.395)$, i.e., point P_3. The associated AMF and characteristic spectra are superposed in Fig. 6(b–d). Clearly, although $h = 6.05 > h_{\min}^{[G]}$ in both cases P_1 and P_3, achieving complete vibration

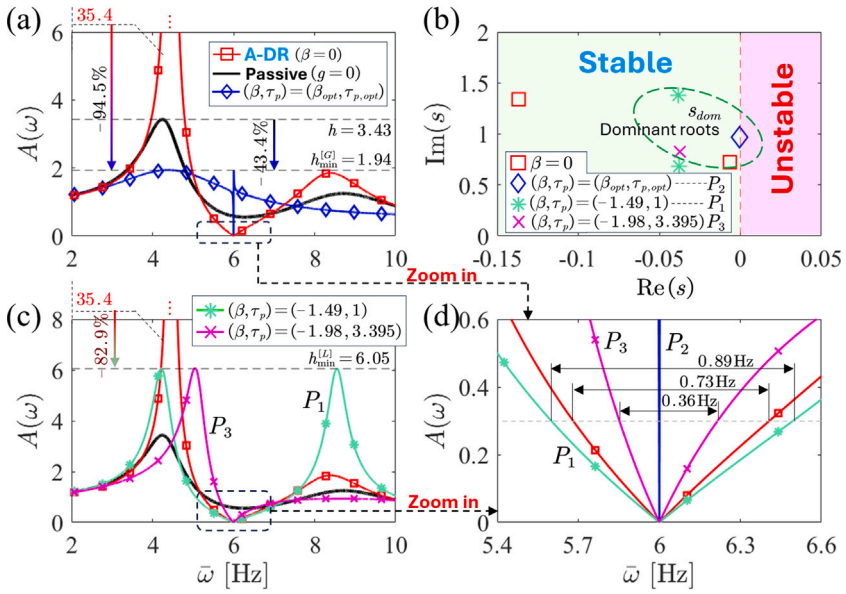

Fig. 6. Specific analyses of the results in Fig. 5 to show the issues when achieving the global minimum of h. (a, c). Variations of the AMF $A(\omega)$ with respect to various pairs of (β,τ_p) in the passive case $g=0$ or in the active case where (g,τ_a) are tuned at $\bar{\omega}_t=6$ Hz. (d). The zoomed plot of (a, c) for the antiresonance valley around ω_t. (b). Spectral distributions of (16) with respect to (β,τ_p) based on the QPmR [70]. Abscissas of (a, c, d) are scaled as $\bar{\omega}=\omega\bar{\omega}_p$. Markers (P_1,P_2,P_3) in (c, d) stem from the namesake ones in Fig. 5.

suppression is much easier when $h=6.05$ from the perspectives of settling time and the width of antiresonance valley. Note that the (β,τ_p) pairs resulting in a h satisfying $h^{[G]}_{\min}<h\leqslant 6.05$ is infinite, as shown in Fig. 5(a, c), where the critical pairs yielding $h=6.05$ are highlighted as green curves. However, we mainly focus on $A^{[E]}(\beta,\tau_p)$ and $A^{[M]}(\beta,\tau_p)$ since the related equal-peak feature and minimum conditions help simplify calculations, as to be further introduced.

5.2. Constrained H_∞ optimization

We have shown that reducing the resonance peak h can be unfavorable to complete vibration suppression by increasing the settling time and narrowing the antiresonance valley at ω_t. Note that such two indices have been taken as optimization objectives to enhance the DR performance [17–19,24]. To this end, we constrain the H_∞ optimization problem (23) as

$$\left(\tilde{\beta}_{opt},\tilde{\tau}_{p,opt}\right)_{\left[\omega_t,\delta^{[up]}_{dom},\delta^{[up]}_{wa},A_v\right]} = \left\{(\beta,\tau_p)\left\{\begin{array}{l}\min\limits_{(\beta,\tau_p)}\left\{h\left(g_t\left(\omega_t\right),\tau_{a,t}\left(\omega_t\right),\beta,\tau_p\right)\right\},\\ s.t.\left\{\begin{array}{l}\delta_{dom}\left(g_t\left(\omega_t\right),\tau_{a,t}\left(\omega_t\right),\beta,\tau_p\right)\leqslant\delta^{[up]}_{dom}<0,\\ \delta_{wa}\left(A_v,g_t\left(\omega_t\right),\tau_{a,t}\left(\omega_t\right),\beta,\tau_p\right)\geqslant\delta^{[low]}_{wa}>0.\end{array}\right.\end{array}\right\},\right. \tag{29}$$

where three new parameters $\left(\delta^{[up]}_{dom},\delta^{[low]}_{wa},A_v\right)$ are introduced to achieve operable complete vibration suppression. Particularly, in (29), $\delta_{dom}=\mathrm{Re}\left(s_{dom}\right)$ signifying the real part of dominant roots is a function of $\left(g_t\left(\omega_t\right),\tau_{a,t}\left(\omega_t\right),\beta,\tau_p\right)$, and $\delta^{[up]}_{dom}<0$ guarantees system stability and limits the maximum settling time. We use the duration of 98% reduction of impact responses to approximate the settling time denoted as t_s,

$$e^{-\delta_{dom}t_s}=0.02\Longleftrightarrow t_s=-4/\delta_{dom}, \tag{30}$$

where $\delta_{dom}<0$. Clearly, a smaller δ_{dom} is preferred, as aforementioned. Besides, δ_{wa} in (29) signifies the width of the antiresonance valley at ω_t, with the definition of

$$\delta_{wa}=\omega_{v,n}-\omega_{v,n-1}, \tag{31}$$

where $\omega_{v,n}, n=1,2,\ldots,N$, stem from

$$\left\{\begin{array}{l}A\left(\omega_{v,n},g_t\left(\omega_t\right),\tau_{a,t}\left(\omega_t\right),\beta,\tau_p\right)=A_v,\\ \omega_{v,1}<\omega_{v,2}<\cdots<\omega_{v,N},\\ \omega_{v,n-1}<\omega_t<\omega_{v,n},\end{array}\right. \tag{32}$$

in which $A_v<1$ needs to be specified. For instance, we have $N=2$ and $\bar{\delta}_{wa}=\delta_{wa}\bar{\omega}_p=0.89$ Hz when $A_v=0.3$ in the case $(\beta,\tau_p)=(-1.49,1)$ considered in Fig. 6(d). Clearly, A_v should be desirably small, and larger values of δ_{wa} and $\delta^{[low]}_{wa}$ benefit complete vibration suppression at ω_t. Note that the minimum of h resulting from Eq. (29), denoted as $\tilde{h}_{\min}$, satisfies $\tilde{h}_{\min}\geqslant h^{[G]}_{\min}$, where $h^{[G]}_{\min}$ is the global minimum resulting from Eq. (23), see also Fig. 5(b) and Fig. 6. Particularly, the analytical expressions of $(h,\delta_{dom},\delta_{wa})$ are unclear, making Eq. (29) a non-convex problem to be handled next.

5.3. Optimization logic and establishment of analytical conditions

5.3.1. Optimization logic

Since the form of h is unclear, the solution $\left(\tilde{\beta}_{opt},\tilde{\tau}_{p,opt}\right)$ cannot be directly obtained. Besides, the nonconservative values of $\left(\delta^{[up]}_{dom},\delta^{[low]}_{wa}\right)$ to benefit complete vibration suppression while making optimization operable are unknown without the brute-force sweeping tests as Fig. 5. To reduce computational loads, we start with determining all the local minima $h^{[L]}_{\min}$ by seeking the associated (β,τ_p) pairs denoted as $\left(\beta^{[L]},\tau^{[L]}_p\right)$ within stable regions since analytical conditions can be established to simplify calculations, as to be addressed. Accordingly, we calculate $(\delta_{dom},\delta_{wa})$ at each pair of $\left(\beta^{[L]},\tau^{[L]}_p\right)$. By checking $(\delta_{dom},\delta_{wa})$ as per the desired $\left(\delta^{[up]}_{dom},\delta^{[low]}_{wa}\right)$, we select $\tilde{h}_{\min}$ from the set of $h^{[L]}_{\min}$. If the obtained $(\delta_{dom},\delta_{wa})$ are unsatisfactory, we then perform numerical sweeping as Fig. 5 to check the cases where h does not appear as a local minimum. If desirable solutions are still unavailable, one should redesign the absorber structure and then repeat the above procedure. The optimization logic is summarized in Fig. 7.

For the coupled system (20), we execute optimization by only determining $\left(\beta^{[L]},\tau^{[L]}_p\right)$ for $h^{[L]}_{\min}$, i.e., block ① of Fig. 7, given that the A-DR can be significantly enhanced at limited computational costs. Note that the simplification by focusing on $h^{[L]}_{\min}$ is based on the fact that

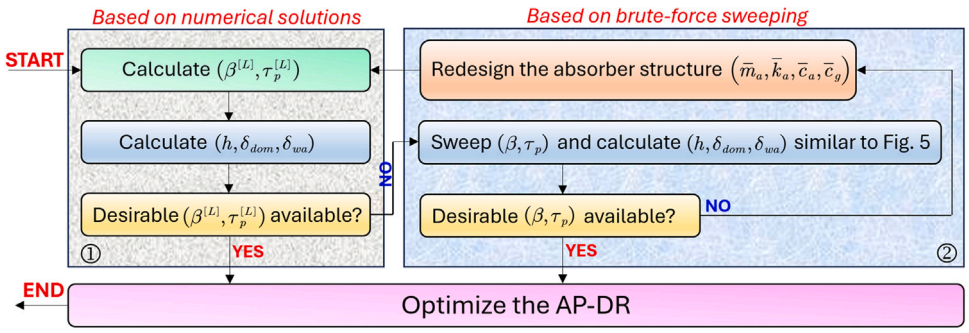

Fig. 7. H_∞ optimization logic of the AP-DR. Numerical solutions are available when following the procedure in block ①, and block ② is an alternative based on brute-force sweeping if desirable solutions are unavailable in block ①.

reducing h is the main task as per the definition of H_∞ optimization, i.e., we do not maximize the performance enhancement resulting from tuning $(\delta_{dom},\delta_{wa})$. This is also the salient difference between this work to control the maximum vibrations excited by perturbations at any frequency different form ω_t and the previous ones [18,24] to enhance complete vibration suppression at ω_t or to reduce residual vibrations caused by a small frequency mismatch from ω_t.

Before determining $\left(\beta^{[L]},\tau_p^{[L]}\right)$, we revisit Fig. 5, where $h_{\min}^{[L]}$ can appear when varying either β or τ_p with fixing the other. Here, we determine $h_{\min}^{[L]}$ while sweeping τ_p (i.e., solve β for a given τ_p), which benefits convergence by avoiding multiple solutions. Given that $h_{\min}^{[L]}$ can also appear when the equal-peak feature does not exist, i.e., (β,τ_p) on curves $A^{[E]}(\beta,\tau_p)$ and $A^{[M]}(\beta,\tau_p)$ can both correspond to $h_{\min}^{[L]}$, the following analyses to determine $h_{\min}^{[L]}$ are twofold separately corresponding to $A^{[E]}(\beta,\tau_p)$ and $A^{[M]}(\beta,\tau_p)$. For discrimination, the self-evident notations $\left(h_{\min}^{[E]},\beta^{[E]}\right)$ and $\left(h_{\min}^{[M]},\beta^{[M]}\right)$ are used to denote such two different cases. Note that the original 2D dense brute-force sweeping of (β,τ_p) in Fig. 5 is now reduced to the much simpler 1D sweeping of τ_p for numerical solutions of explicit equations.

5.3.2. Determining $h_{\min}^{[E]}$ based on the equal-peak feature

Since $h_{\min}^{[E]}$ is a function of $(\beta^{[E]},\tau_p)$ when $(g,\tau_a)=(g_t(\omega_t),\tau_{a,t}(\omega_t))$, the task is to determine $\beta^{[E]}$ yielding the equal-peak feature for a given τ_p. Based on the condition that two resonance peaks are at the same height, we have

$$\begin{aligned}&\left(\omega_{r1}^{[E]},\omega_{r2}^{[E]},\beta^{[E]}\right)_{[\omega_t,\tau_p]}\\&=\left\{(\omega_1,\omega_2,\beta)\left|\begin{array}{l}\frac{\partial A^2(\omega,\beta)}{\partial\omega}\,|_{\omega=\omega_1}=0,\\ \frac{\partial A^2(\omega,\beta)}{\partial\omega}\,|_{\omega=\omega_2}=0,\\ A^2(\omega_1,\beta)=A^2(\omega_2,\beta),\\ s.t.:\left\{\begin{array}{l}Cond.1:A^2(\omega,\beta)\leqslant A(\omega_1,\beta),\\ Cond.2:\frac{\partial A^2(\omega_1,\beta)}{\partial\beta}\times\frac{\partial A^2(\omega_2,\beta)}{\partial\beta}<0\end{array}\right.\end{array}\right.\right\}.\end{aligned}\tag{33}$$

where $\left(\omega_{r1}^{[E]},\omega_{r2}^{[E]}\right)$ denote the two frequencies related to the two equal resonance peaks, $(g,\tau_a)=(g_t(\omega_t),\tau_{a,t}(\omega_t))$ and τ_p are omitted on the right, and the AMF $A(\omega,\beta)$ appears in the square form for rationalization. Besides, the first constraint condition requires that the equal-peak feature is achieved at the maximum of $A(\omega,\beta)$, and the second one corresponds to the local minimum condition of $h_{\min}^{[E]}$. Particularly, $A^2(\omega,\beta)$ has the fractional form of

$$A^2(\omega,\beta)=\frac{N(\omega)}{D(\omega,\beta)},\tag{34}$$

where N and D are two polynomials following

$$\begin{cases}N(\omega)=\sum_{i=0}^{4}\alpha_i(C_a,C_p,S_a,S_p)\omega^i,\\ D(\omega,\beta)=\sum_{i=0}^{8}\gamma_i(\beta,C_a,C_p,S_a,S_p)\omega^i,\end{cases}\tag{35}$$

in which α_i and γ_i are polynomial coefficients parameterized in β, $C_a=\cos(\tau_{a,t}\omega)$, $S_a=\sin(\tau_{a,t}\omega)$, $C_p=\cos(\tau_p\omega)$, and $S_p=\sin(\tau_p\omega)$. The extremum condition $\partial A^2(\omega,\beta)/\partial\omega=0$ in (33) is then equivalent to

$$\frac{\partial N(\omega)}{\partial\omega}D(\omega,\beta)-N(\omega)\frac{\partial D(\omega,\beta)}{\partial\omega}=0.\tag{36}$$

From the form of (35), determining $\beta^{[E]}$ while sweeping τ_p rather than the inverse reduces equation complexities since τ_p appears in the transcendental terms (C_p,S_p), in addition to avoiding multiple solutions. Eq. (33) governs three variables $(\omega_1,\omega_2,\beta)$ in three explicit equations and thus is solvable.

5.3.3. Determining $h_{\min}^{[M]}$ based on the minimum condition of a single resonance peak

Next, we determine $\beta^{[M]}$ related to $h_{\min}^{[M]}$. According to the curve $A^{[M]}(\beta,\tau_p)$ in Fig. 5, as β varies while fixing τ_p, $h_{\min}^{[M]}$ appears requiring that the corresponding resonance peak is a local minimum with respect to (ω,β). Therefore, we consider

$$\frac{\partial A^2(\omega,\beta)}{\partial(\omega,\beta)}=\frac{\partial A^2(\omega,\beta)}{\partial\omega}d\omega+\frac{\partial A^2(\omega,\beta)}{\partial\beta}d\beta=0,\tag{37}$$

which should hold regardless of whether $d\omega=0$ or $d\beta=0$. To this end, $\beta^{[M]}$ can be determined as per

$$\left(\omega_r^{[M]},\beta^{[M]}\right)_{[\omega_t,\tau_p]}=\left\{(\omega_1,\beta)\left|\begin{array}{l}\frac{\partial A^2(\omega,\beta)}{\partial\omega}\,|_{\omega=\omega_1}=0,\\ \frac{\partial A^2(\omega,\beta)}{\partial\beta}\,|_{\omega=\omega_1}=0,\\ s.t.:A^2(\omega,\beta)\leqslant A(\omega_1,\beta).\end{array}\right.\right\},\tag{38}$$

where $\omega_r^{[M]}$ is the corresponding resonance frequency; $(g,\tau_a)=(g_t(\omega_t),\tau_{a,t}(\omega_t))$ and τ_p are given and thus are omitted on the right similar to (33). In this case, one can conclude from the form of (34) that

$$\frac{\partial A^2(\omega,\beta)}{\partial\beta}=0\Leftrightarrow\frac{-N(\omega)}{D^2(\omega,\beta)}\frac{\partial D(\omega,\beta)}{\partial\beta}=0.\tag{39}$$

Given that $N\neq0$ otherwise $A=0$, the equation $\partial A^2(\omega,\beta)/\partial\beta=0$ in (38) can be simplified as

$$\frac{\partial A^2(\omega,\beta)}{\partial\beta}=0\rightarrow\frac{\partial D(\omega,\beta)}{\partial\beta}=\sum_{i=0}^{6}\kappa_i(\beta,C_a,C_p,S_a,S_p)\omega^i=0,\tag{40}$$

where κ_i are real polynomial coefficients in (β,C_a,C_p,S_a,S_p), see (36) for $\partial A^2(\omega,\beta)/\partial\omega=0$.

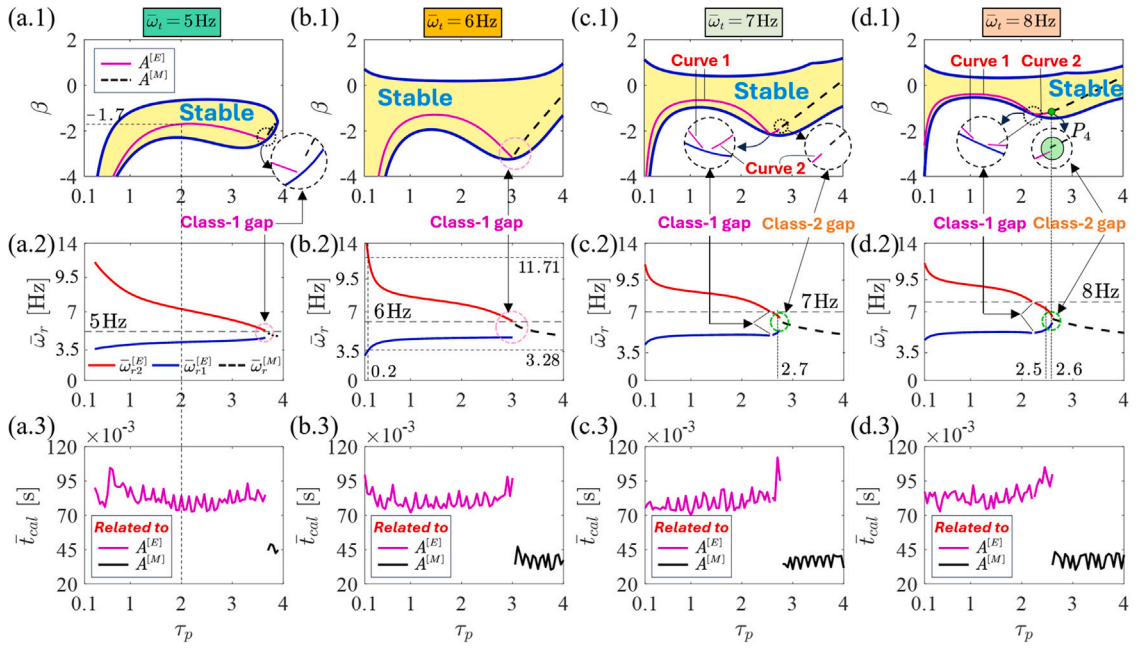

Fig. 8. Stable solutions of Eqs. (33) and (38). (a). $\bar{\omega}_t = 5$ Hz. (b). $\bar{\omega}_t = 6$ Hz. (c). $\bar{\omega}_t = 7$ Hz. (d). $\bar{\omega}_t = 8$ Hz. In all cases, $(g_t, \tau_{a,t})$ are tuned at the branch $(g_t < 0, b = 1)$. First row (a.1, b.1, c.1, d.1): Variations of $(\beta^{[E]}, \beta^{[M]})$ versus τ_p. Colored regions are stable, which can be obtained similarly to Fig. 3. Second row: Variations of resonance frequencies $\left(\omega_{r1}^{[E]}, \omega_{r2}^{[E]}, \omega_r^{[M]}\right)$ versus τ_p. Last row: Time costs for solving Eqs. (33) and (38).

Remark 4. A proper initial guess benefits the desirable convergence of numerical solutions. To obtain the initial guesses of $(\omega_1, \omega_2, \beta)$ in (33) and (ω_1, β) in (38), we can utilize the continuity of the two curves $A^{[E]}(\beta, \tau_p)$ and $A^{[M]}(\beta, \tau_p)$ by recursively solving Eqs. (33) and (38), i.e., solutions at the last step of τ_p are used as the initial guess at the current step. The starting initial guess is available by sweeping β. Besides, continuous $A^{[E]}(\beta, \tau_p)$ and $A^{[M]}(\beta, \tau_p)$ correspond to continuous variations of $(\beta^{[E]}, \beta^{[M]})$, and operable solutions $(\beta^{[E]}, \beta^{[M]})$ must lie within stable regions, in which the stable interval of β for a given τ_p can be known from the stability boundaries $(\beta_c, \tau_{p,c})$ in (27). ■

6. Results

The results demonstrated in this section are twofold: (1). Distributions of the solutions $(\beta^{[E]}, \beta^{[M]})$ of Eqs. (33) and (38) for different tuning frequencies ω_t. (2). Enhanced vibration suppression performance by the optimized AP-DR compared with the classical A-DR. As a further step from Section 5, we only consider the branch $(g_t < 0, b = 1)$ when tuning $(g_t, \tau_{a,t})$.

6.1. Optimization results and analysis

The optimization following (33) and (38) in four cases $\bar{\omega}_t = [5, 6, 7, 8]$ Hz is considered in Fig. 8, which only depicts the variations of stable solutions $(\beta^{[E]}, \beta^{[M]})$ and the associated resonance frequencies $\left(\omega_{r1}^{[E]}, \omega_{r2}^{[E]}, \omega_r^{[M]}\right)$ with respect to τ_p. Note that results in Fig. 8(b) for $\bar{\omega}_t = 6$ Hz concur with Fig. 5. Accordingly, Fig. 8(a.3, b.3, c.3, d.3) show the computational time costs denoted as $\bar{t}_{cal}$ when solving Eqs. (33) and (38), which is performed on MATLAB 2023a (with an i9-13900HX CPU and a 16 GB RAM) and is measured by the embedded command $tic{-}toc$. The sufficiently reduced time costs compared with the previous brute-force sweeping tests in Fig. 5, which only yield approximate solutions at a heavy time cost ($\bar{t}_{cal} > 400$ s when the grid space in both directions of (β, τ_p) is 0.05), benefit the real-time or online optimization of the AP-DR.

Let us now focus on the first two rows of Fig. 8, and several common observations are discussed. First, the class-1 gaps as marked stem from the artificial solution truncations to focus on stable solutions and thus to reduce the number of checks for $(\delta_{dom}, \delta_{wa})$. Second, the gap between $A^{[E]}$ and $A^{[M]}$ when it is independent of stability, which is marked as the class-2 gap, results from the discontinuity between such two curves. That is, eliminating the class-2 gap requires that $A^{[E]} = A^{[M]}$, i.e., Eqs. (33) and (38) simultaneously hold for the same pair of (β, τ_p), see P_4 in Fig. 8(d.1, d.2) for the approximate case $A^{[E]} \approx A^{[M]}$ when $\beta^{[E]} \approx \beta^{[M]} = -1.15$ at $\tau_p = 2.6$. Third, the two equal resonance peaks do not necessarily lie on the two sides of the tuning frequency ω_t. From Fig. 8(c.1, d.1), two curves of $A^{[E]}$ exist for each ω_t, as marked by Curves 1 and 2. As accordingly shown in Fig. 8(c.2, d.2), the two resonance frequencies $\left(\omega_{r1}^{[E]}, \omega_{r2}^{[E]}\right)$ related to Curve 2 both lie on the left side of ω_t. More specifically, we consider two cases, i.e., $(\beta^{[E]}, \tau_p) = (-2, 2.7)$ for $\bar{\omega}_t = 7$ Hz and $(\beta^{[E]}, \tau_p) = (-1.225, 2.5)$ for $\bar{\omega}_t = 8$ Hz. The resulting self-evident AMF curves $A(\omega)$ are shown in Fig. 9.

At last, Fig. 8 shows that as the curve $A^{[E]}$ approaches stability boundaries $(\beta_c, \tau_{p,c})$, it corresponds to the condition $\omega_r \approx \omega_t$. From the forms of (16) and (34), one has $D(\omega_c, \beta_c, \tau_{p,c}) = 0$, and thus the resonance frequency at $\omega_r = \omega_c$ leads to $A(\omega_r, \beta_c, \tau_{p,c}) \to \infty$. If the equal-peak optimization is operable and yields $(\beta^{[E]}, \tau_p) \approx (\beta_c, \tau_{p,c})$, then $A(\omega_r, \beta^{[E]})$ must be limited since the co-existence of two infinite resonance peaks is not allowed when $(\beta_c, \tau_{p,c})$ correspond to a single pair of imaginary roots $s = \pm j\omega_c$. Thus, it requires that $\omega_r \approx \omega_t$ so that $N(\omega_r) \approx 0$ neutralizes the effects of $D(\omega_r, \beta^{[E]}, \tau_p) \approx 0$. Note that $(g, \tau_a) = (g_t(\omega_t), \tau_{a,t}(\omega_t))$ as per (8).

6.2. Enhanced vibration suppression

Having obtained the stable solutions $(\beta^{[E]}, \beta^{[M]})$ as Fig. 8, we now evaluate the enhanced vibration suppression performance by adopting an optimized AP-DR. The evaluation follows Section 5.2, i.e., reducing the resonance peak h should not pose significant negative effects to complete vibration suppression. Three indices $(h, \delta_{dom}, \delta_{wa})$ are considered, in which we select $A_v = 0.3$ for δ_{wa} according to Eqs. (31) and (32). The results for $\bar{\omega}_t = [5, 6, 7, 8]$ Hz are shown in Fig. 10.

From Fig. 10(a.2, b.2, c.2, d.2), which show the variations of the real part of the dominant roots s_{dom} of Eq. (16), the AP-DR tuned with

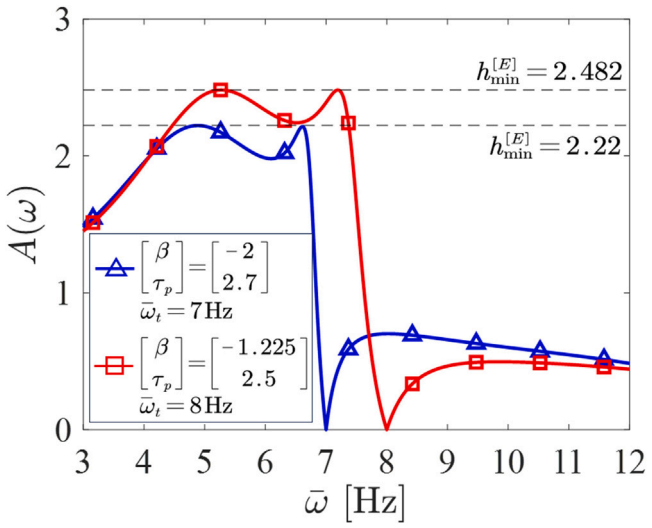

Fig. 9. Demonstration of the special cases of the optimum solutions in Fig. 8, i.e., the equal resonance peaks of the optimized AMF curves $A(\omega)$ can lie on the same side of the tuning frequency $\bar{\omega}_t$. Abscissa is scaled as $\bar{\omega} = \omega\bar{\omega}_p$.

the obtained stable solutions $(\beta^{[E]}, \beta^{[M]})$ and the corresponding τ_p do not destabilize the coupled system, i.e., $\delta_{dom} < 0$, verifying the stability maps in Fig. 3. Note from Fig. 10(a.2) that the system in the A-DR case for $\bar{\omega}_t = 5$ Hz is unstable, agreeing with Fig. 2(b), and stability can be recovered by adopting the optimized AP-DR, as aforementioned in Section 4.3. On the other hand, the cases $\delta_{dom} \to 0$ in Fig. 10 correspond to the truncations of $(A^{[E]}, A^{[M]})$ by stability boundaries $(\beta_c, \tau_{p,c})$, which are expected since $(\beta_c, \tau_{p,c})$ correspond to imaginary roots $s = \pm j\omega_c$, as discussed in Fig. 8.

Next, we focus on Fig. 10(b–d) for the cases $\bar{\omega}_t = [6, 7, 8]$ Hz, where the system in both the A-DR and AP-DR cases is stable. For reducing h in the A-DR case by adopting the AP-DR, the reduction can reach up to 94.5%, 83.7%, and 69% when $\bar{\omega}_t = 6$ Hz, $\bar{\omega}_t = 7$ Hz, and $\bar{\omega}_t = 8$ Hz, respectively, as marked in Fig. 10(b.1, c.1, d.1). However, pursuing such extremum reductions is practically inoperable, given that it corresponds to either $\delta_{dom} \approx 0$ or $\bar{\delta}_{wa} \approx 0$, which significantly deteriorates the performance of complete vibration suppression at $\bar{\omega}_t$. Since smaller values of $(h, \delta_{dom} < 0)$ and a larger δ_{wa} are preferred, the regions where such three indices are all enhanced compared with those in the A-DR case are highlighted as the AE (all-enhanced) region. The AE region guides the selection of τ_p for optimization, and the width of the AE regions is mainly limited by δ_{wa}. Within the AE regions, we seek the maximum reduction of h, leading to 85.7%, 57.9%, and 33.3% reductions when $\tau_p = 1.6$ for $\bar{\omega}_t = 6$ Hz, $\tau_p = 1.3$ for $\bar{\omega}_t = 7$ Hz, and $\tau_p = 3.15$ for $\bar{\omega}_t = 8$ Hz, respectively, as marked in Fig. 10. Note that the reductions of h are still significant and that achieving them also beneficially reduces δ_{dom} without narrowing δ_{wa}, leading to 86.4%, 29.3%, and 42% reductions of the settling time t_s in such three cases as per the definition (30). More intuitively, the related spectra and the AMF $A(\omega)$ are shown in Fig. 11.

From Fig. 11(a.1, b.1, c.1), the dominant roots s_{dom} in the optimized AP-DR cases lie further than those in the A-DR case on the left half of the complex plane, agreeing with the distributions of δ_{dom} shown in Fig. 10(b.2, c.2, d.2). The significantly reduced resonance peaks by adopting the optimized AP-DR can be found in Fig. 11(a.2, b.2, c.2). Besides, from the zoomed plots in Fig. 11(a.2, b.2, c.2), the optimized AP-DR does not narrow the antiresonance valleys at ω_t of the A-DR, as expected. Fig. 11(c) shows that the AE regions can also correspond to the case without the equal-peak feature, agreeing with Fig. 10(d).

On the other hand, if the mismatch between the actual frequency ω and the detected one ω_t is small or residual vibrations are small, one can further reduce δ_{dom} to expedite response speed by compromising a slightly reduced δ_{wa} according to Fig. 10. Similarly, if one expects to enhance the suppression of residual vibrations, δ_{wa} can be further increased by lowering the requirements on δ_{dom}. Note from Fig. 10 that h can be further reduced in both cases. Particularly, the performance of the A-DR is taken as the benchmark in the above discussions to determine the pairs (β, τ_p) for optimizing the AP-DR. Alternatively, with Fig. 10, one can also select (β, τ_p) based on the desired bounds $\left(\delta_{dom}^{[up]}, \delta_{wa}^{[low]}\right)$ following (29), which, however, is not exemplified in this work to focus on the comparisons between the A-DR and AP-DR.

7. Case studies

Simulations and experiments are conducted in this section to verify the claimed benefits of the AP-DR compared with the classical A-DR, including the extended operable low-frequency band, reduced resonance peaks, and enhanced complete vibration suppression. The SIMULINK-based simulation models and video recordings of experiments can be found in Appendix.

7.1. Experimental setup

The experimental setup following Fig. 1 is shown in Fig. 12. The mechanical body is depicted in Fig. 12(a, b), which is mainly constituted by two platforms respectively acting as the primary structure and the absorber. Two voice coil motors (VCMs) are used to separately generate the excitation $\bar{f}_e$ (by VCM1) and the feedback actuation force $\bar{u}$ (by VCM2), and two laser sensors are fixed on the frame to monitor the absolute displacement of the primary structure and the absorber. Each VCM consists of a stator (magnet) and a mover (coil) and takes effect based on the electromagnetic effect. The hardware loop for driving VCM2 is shown in Fig. 12(c), where the dSPACE MicroLabBox serves as the controller, and the VCM driver (SDS01-A010CA) linearly converts the control signal in analog voltage to the current input to VCM2, thus yielding the desired coupling forces between the VCM mover and stator. Based on measurements and system identification, the mechanical system parameters are obtained as

$$\begin{aligned}&\bar{m}_a = 0.51\ \text{kg}, \bar{c}_a = 4.3\ \text{Ns/m}, \bar{c}_g = 2.0\ \text{Ns/m}, \bar{k}_a = 753\ \text{N/m},\\ &\bar{m}_p = 0.965\ \text{kg}, \bar{c}_p = 5.0\ \text{Ns/m}, \bar{k}_p = 1465\ \text{N/m},\end{aligned} \tag{41}$$

which correspond to the dimensionless parameters in (20) as per (2). Besides, the sampling frequency is 1 kHz. Following Sections 5 and 6, we only consider the tuned pair $(g_t, \tau_{a,t})$ at the branch $(g_t < 0, b = 1)$ in the tests. Note that $(\bar{g}, \bar{\tau}_a, \bar{\tau}_p) = (g\bar{k}_p, \tau_a/\bar{\omega}_p, \tau_p/\bar{\omega}_p)$ and that the two delays should be corrected as per Remark 1 ($\bar{t}_{loop} = 1$ ms is adopted here).

7.2. Case 1: Complete vibration suppression and extended operable low-frequency band

From Fig. 10(a.2), the A-DR cannot achieve complete vibration suppression at $\bar{\omega} = 5$ Hz due to instability. However, experimentally observing the unstable dynamics at such a low frequency is not allowed as the rapidly diverging system responses significantly exceed the operable working space thus leading to collisions. As per the numerical method in [17], the tuned A-DR destabilizes the system when $\bar{\omega}_t \leqslant 5.76$ Hz. To this end, we consider the case $\bar{\omega}_t = \bar{\omega} = 5.7$ Hz to test the instability, yielding $(g_t, \tau_{a,t}) = (-0.168, 2.158)$ or $(\bar{g}_t, \bar{\tau}_{a,t}) = (-246.331\ \text{N/m}, 55.4\ \text{ms})$. When $|\bar{f}_e| = 4$ N, the resulting unstable responses of the primary structure in simulations and experiments are shown as the blue divergent curves in Fig. 13(a) and (c), respectively.

By alternatively deploying the AP-DR, the desired complete vibration suppression at the low frequency $\bar{\omega} = 5$ Hz can be achieved. In this

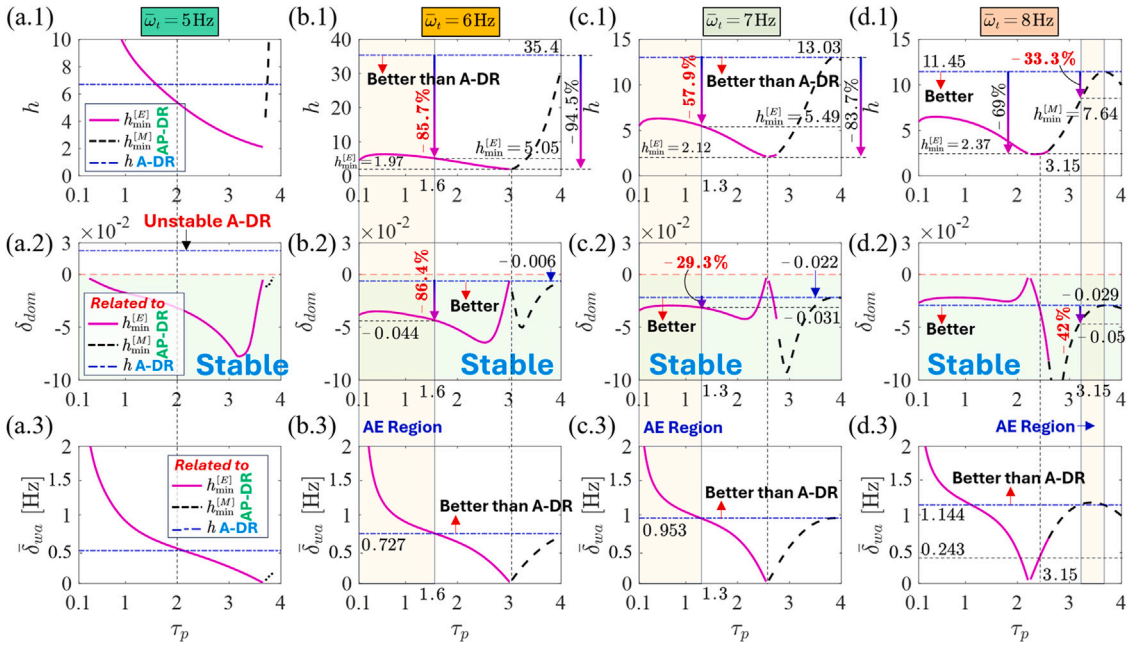

Fig. 10. Comparisons between the A-DR ($\beta = 0$) and the AP-DR optimized by $(\beta^{[E]}, \beta^{[M]})$ obtained in Fig. 8. (a). $\bar{\omega}_t = 5$ Hz. (b). $\bar{\omega}_t = 6$ Hz. (c). $\bar{\omega}_t = 7$ Hz. (d). $\bar{\omega}_t = 8$ Hz. In all cases, $(g_t, \tau_{a,t})$ are tuned at the branch $(g_t < 0, b = 1)$. First row (a.1, b.1, c.1, d.1): Variations of resonance peak h versus τ_p. Second row: Variations of δ_{dom} versus τ_p. Last row: δ_{wa} versus τ_p when $A_v = 0.3$. $(\delta_{dom}, \delta_{wa}, A_v)$ signifying the complete vibration suppression performance are defined in Section 5.2.

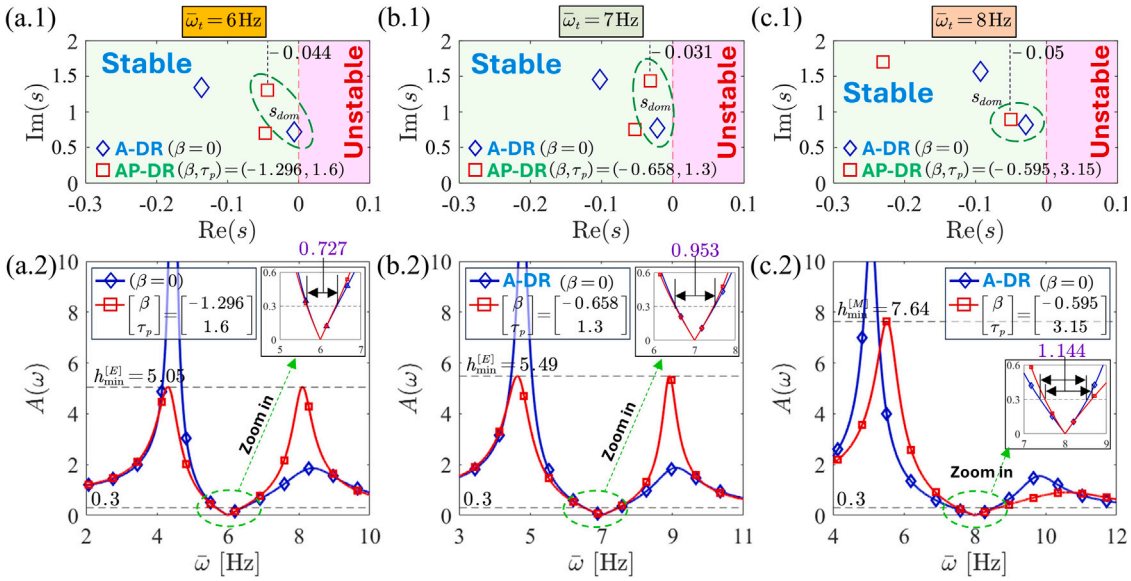

Fig. 11. Comparisons between the A-DR ($\beta = 0$) and the AP-DR optimized by $(\beta^{[E]}, \beta^{[M]})$. (a). $\bar{\omega}_t = 6$ Hz. (b). $\bar{\omega}_t = 7$ Hz. (c). $\bar{\omega}_t = 8$ Hz. First row (a.1, b.1, c.1): Spectra of Eq. (16). Second row: Variations of the AMF $A(\omega)$, with abscissas scaled as $\bar{\omega} = \omega\bar{\omega}_p$. The (β, τ_p) pairs for optimizing the AP-DR stem from Fig. 10. $(g_t, \tau_{a,t})$ are tuned at the branch $(g_t < 0, b = 1)$.

case, the tuned pair becomes $(\bar{g}_t, \bar{\tau}_{a,t}) = (-318.57\ \text{N/m}, 78.7\ \text{ms})$, and we select $\beta = -1.7$ and $\tau_p = 2$ ($\bar{\tau}_p = 51.3$ ms) in light of Fig. 8(a.1). The ideal complete vibration suppression $|\bar{x}_p| \equiv 0$ can be found in simulations shown as the red solid curves in Fig. 13(a), see also Fig. 13(b) for the root mean square (RMS) of all $\bar{x}_p$ grids dynamically sampled at the last 400 time steps. The experimental complete vibration suppression is shown in Fig. 13(c, d), where the AP-DR suppresses vibrations in the passive case by more than 90%. The small residual vibrations stem from noises and implementation errors of $\bar{u}$. Hence, the AP-DR extends the operable low-frequency band of the A-DR by $1 - 5/5.76 = 13.2\%$ at least. Exactly determining the extension is left to another report since the main task here is to reduce the resonance peak h as shown next.

7.3. Case 2: Reduced resonance peak by optimizing the AP-DR

Fig. 13 shows that theoretical results well predict system responses under single-frequency excitations. We here test the capacity of the AP-DR for manipulating the frequency response function to reduce the resonance peak h. Let us now consider the case $\bar{\omega}_t = 6$ Hz, yielding $(\bar{g}_t, \bar{\tau}_{a,t}) = (-239.17\ \text{N/m}, 44.8\ \text{ms})$. In simulation, we apply a random excitation following Fig. 14(a), and the AP-DR is optimized by $(\beta, \bar{\tau}_p) = (-1.296, 41.1\ \text{ms})$ as per Fig. 11(a). The resulting responses $\bar{x}_p$ in the A-DR and AP-DR cases are compared in Fig. 14(b), and the corresponding AMF curves $A(\omega)$ are estimated using tfestimate function of MATLAB as the hollow circles in Fig. 14(c), where the AMF is verified and the zero

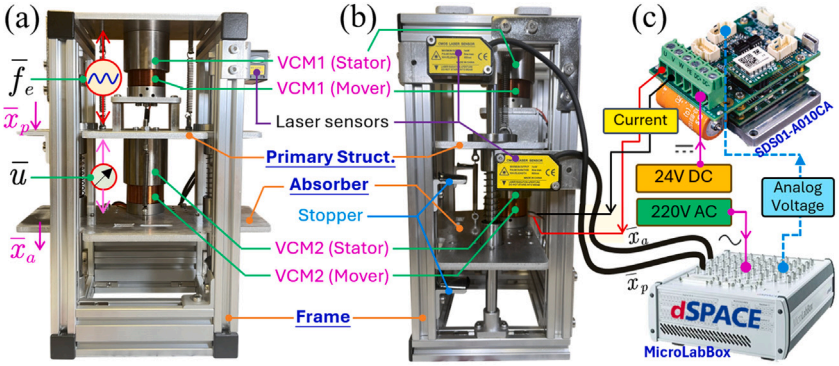

Fig. 12. Experimental setup. Front (a) and right (b) views of the main body. (c). Hardware loop for driving the feedback actuator.

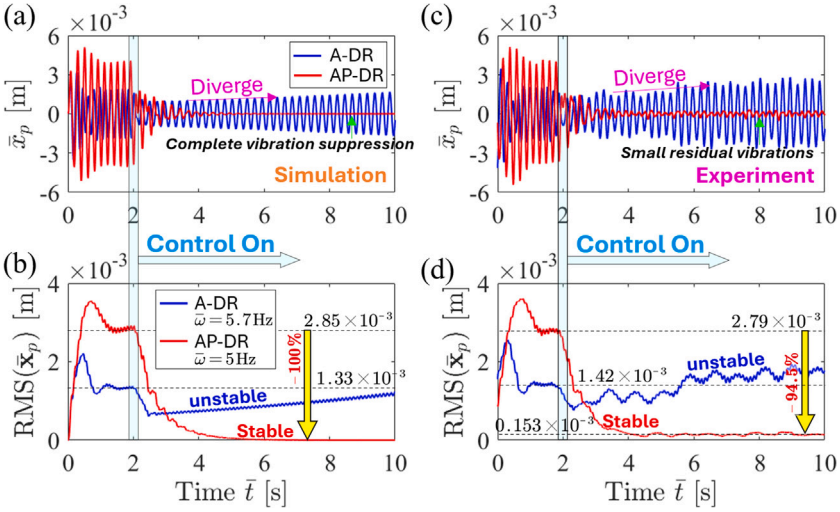

Fig. 13. Simulation (a, b) and experimental (c, d) tests for complete vibration suppression and the accordingly extended operable low-frequency band of the AP-DR compared with the A-DR. (a, c). Time history of $\bar{x}_p$. (c, d). RMS of the sampling grids of $\bar{x}_p$ at last 400 time steps before $\bar{t}$. A-DR is with $\beta = 0$, and $(\beta, \bar{\tau}_p) = (1.7, 51.3\ \text{ms})$ are adopted for the AP-DR.

antiresonance at $\bar{\omega}_t$ appears as expected. Clearly, the AP-DR effectively alters system frequency responses, and the H_∞ optimization effectively reduces the resonance peak h. Note that the reduced h is also reflected in Fig. 14(b), where the maximum amplitude $|\bar{x}_p|$ in the AP-DR case is smaller than that in the A-DR case. However, experimental tests for this part are omitted since the adopted VCM driver is not adept at tracking rapidly changing signals and since $\bar{f}_e$ is generated by manipulating the VCM current via an open loop.

Next, we consider a more specific case to illuminate the original motivation of this work. We let the harmonic excitation $\bar{f}_e$ of $(\bar{\omega}, |\bar{f}_e|) = (6\ \text{Hz}, 4\ \text{N})$ be perturbated by a small periodic force, which is denoted as $\bar{f}_p$ and is of 10% amplitude (i.e., $|\bar{f}_p| = 0.4$ N), during a short period ($\bar{t} \in [9\ \text{s}, 11\ \text{s}]$). Moreover, $\bar{f}_p$ is at $\bar{\omega} = 4.5$ Hz, which corresponds to the highest resonance peaks in both the A-DR and AP-DR cases as per Fig. 14(b). The time history of the resulting perturbated excitation force $\bar{f}_e$ is shown in Fig. 15(a), and the corresponding responses of the primary structure are recorded in Fig. 15(b–e).

The time interval $\bar{t} \in [2\ \text{s}, 9\ \text{s}]$ of the simulation results in Fig. 15(b, c) shows that tuned feedback control again helps achieve the desired complete vibration suppression. However, once a perturbation $\bar{f}_p$ at the resonance frequency is introduced, the tuned A-DR amplifies the resulting vibrations. From Fig. 15(b), the amplitude $|\bar{x}_p|$ is increased by up to 130% compared with that in the passive case, even if $\bar{f}_p$ is small and lasts shortly. In contrast, the optimized AP-DR limits the raised amplitude $|\bar{x}_p|$ by resulting in 68.9% reduction of the maximum vibration amplitude, thus significantly reducing the risks of structural failures in the cases with perturbations. Similar conclusions can also be obtained from the experimental results in Fig. 15(d, e).

7.4. Case 3: Enhanced complete vibration suppression by optimizing the AP-DR

In addition to reducing the maximum amplitude of $|\bar{x}_p|$, we can find from Fig. 15(b–e) that the convergence of system dynamics to steady states is much faster in the optimized AP-DR case. According to Fig. 10(b.2), we have $\delta_{dom}^{[A]} = -0.006$ for the A-DR and $\delta_{dom}^{[AP]} = -0.044$ for the considered optimized AP-DR, leading to the corresponding settling time defined in (30) as $\bar{t}_s^{[A]} = t_s^{[A]}/\bar{\omega}_p = 17.11$ s and $\bar{t}_s^{[AP]} = 2.33$ s in such two cases. Since $\bar{t}_s^{[A]}$ is unduly long, only $\bar{t}_s^{[AP]}$ is marked in Fig. 15(b–e), where the theoretical settling time $\bar{t}_s$ based on the dominant roots of the characteristic Eq. (16) agrees with system responses. Hence, the optimized AP-DR enhances the complete vibration suppression by expediting the transient process.

On the other hand, note from Fig. 15(d, e) that non-negligible residual vibrations exist in the steady states of experimental results. Such residual vibrations may stem from system noises, inaccurate tuned control parameters $(\bar{g}_t, \bar{\tau}_{a,t})$ due to inaccurate knowledge of system parameters, small frequency mismatch $\bar{\omega} \neq \bar{\omega}_t$, etc. Particularly, the AMF $A(\omega)$ should not vary much if such parametric inaccuracies are limited, which is the case for the considered experimental setup to satisfy linearity. Clearly, reducing the sensitivity of $|\bar{x}_p|$ by extending the antiresonance band at $\bar{\omega}_t$, signified by $\bar{\delta}_{wa}$ as per (31), helps

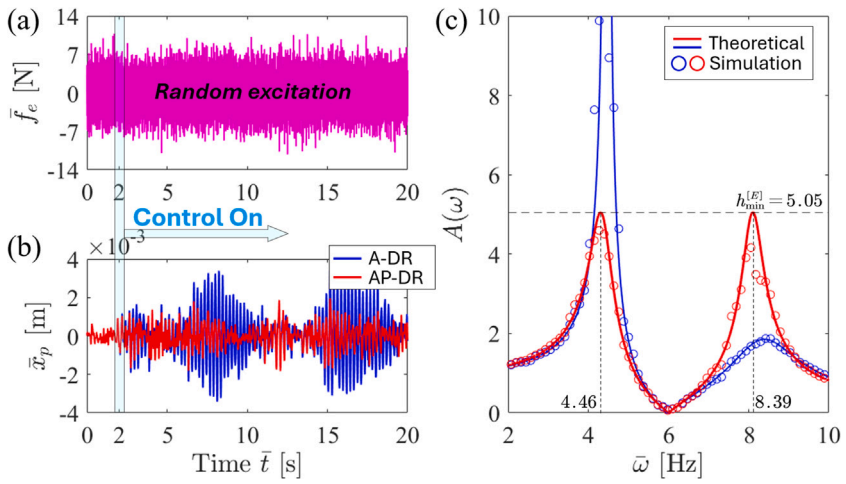

Fig. 14. Verification of the manipulation of frequency responses by the AP-DR. (a). Random excitation with amplitude of 4 N, mean value of 0, variance of 0.5, and sampling time of 1 ms. (b). Time history of $\bar{x}_p$. (c). Estimation of the AMF $A(\omega)$ based on the results in (a) and (b), in which only the data recordings within $\bar{t} \in [2\text{ s}, 20\text{ s}]$ are used.

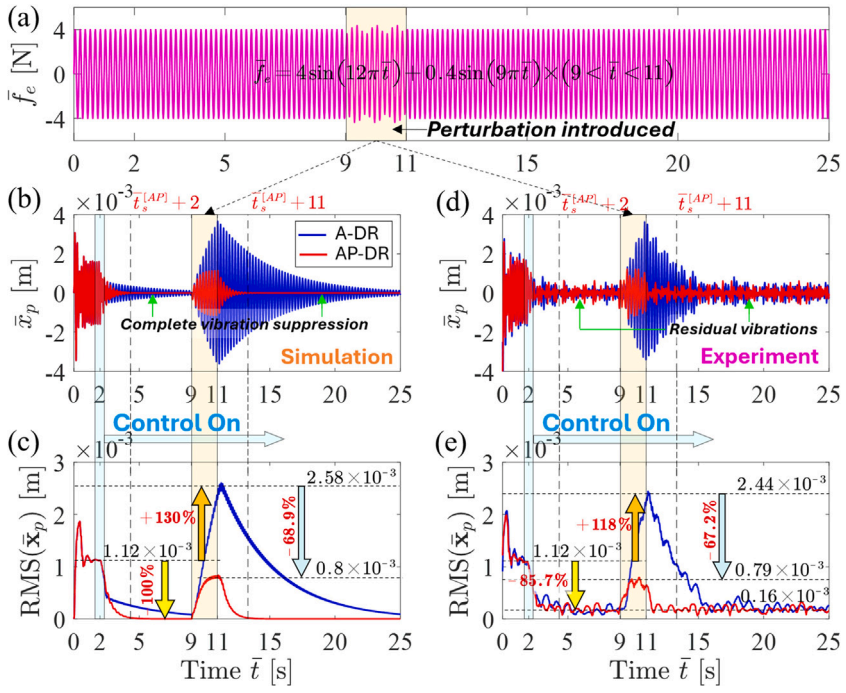

Fig. 15. Verification of suppressing the vibrations caused by force perturbations at the resonance frequency by the AP-DR. (a). Perturbated excitation: $\bar{f}_e = 4\sin(12\pi\bar{t}) + 0.4\sin(9\pi\bar{t}) \times (9 < \bar{t} < 11)$. (b, c). Time history of $\bar{x}_p$. (d, e). RMS of $\bar{x}_p$ grids sampled at last 400 time steps before $\bar{t}$. A-DR is with $\beta = 0$, and $(\beta, \bar{\tau}_p) = (-1.296, 41.1\text{ ms})$ are adopted for the AP-DR.

suppress residual vibrations. For the given case $\bar{\omega} = 6$ Hz, we revisit Fig. 10(b), where $\bar{\delta}_{wa}$ can be extended by reducing $\bar{\tau}_p$ from $\bar{\tau}_p = 41.1$ ms (i.e., $\tau_p = 1.6$) while optimizing β. Furthermore, such an extension poses limited effects on the reduction of h and the settling time $\bar{t}_s$. Note that $(h, \bar{\delta}_{dom}, \bar{\delta}_{wa})$ all vary within the AE region during such a process. To this end, we reduce τ_p from $\tau_p = 1.6$ to $\tau_p = 0.2$ while optimizing β, leading to variations of $(\bar{\tau}_p, \beta)$ shown in Fig. 16(a, b).

The A-DR and optimized AP-DR take effect when $\bar{t} \in [2\text{ s}, 5\text{ s}]$ and $\bar{t} > 5$ s, respectively. From the system responses recorded in Fig. 16(c, d), it is evident that vibrations in the A-DR case start to decrease at an accelerated rate from $\bar{t} = 5$ s onwards with the activation of the optimized AP-DR. When $\bar{t} \in [13\text{ s}, 18\text{ s}]$, where experimental responses arrive at steady states, vibrations in the passive are reduced by 93.8%. We point out that such a reduction ratio is good enough to claim the complete vibration suppression since the test is performed around the natural frequency of the absorber, i.e., $\bar{\omega} \approx \bar{\omega}_a$. Compared with the experimental results RMS $(\bar{\mathbf{x}}_p) = 0.16 \times 10^{-3}$ in Fig. 15, residual vibrations are reduced by $1 - 0.07/0.16 = 56\%$ as expected thanks to increasing $\bar{\delta}_{wa}$. To test that this does not significantly affect $(h, \bar{\delta}_{dom})$, we introduce a perturbation of 10% amplitude and at the resonance frequency $\bar{\omega} = 3.28$ Hz (see Fig. 8(b.2)) when $\bar{t} \in [18\text{ s}, 20\text{ s}]$ similar to Fig. 15. Clearly from the time interval $\bar{t} > 20$ s, excited vibrations are limited and are decreased fast enough. Hence, by properly designing $(\bar{\tau}_p, \beta)$, system performance governed by $(h, \bar{\delta}_{dom}, \bar{\delta}_{wa})$ can all be significantly improved.

8. Conclusions

This work proposes and addresses the H_∞ optimization problem of the DR, aiming to limit the raising of resonance peaks while achieving zero antiresonance for complete vibration suppression. To this end, we adopt a hybrid multiple-delayed control law consisting of delayed states

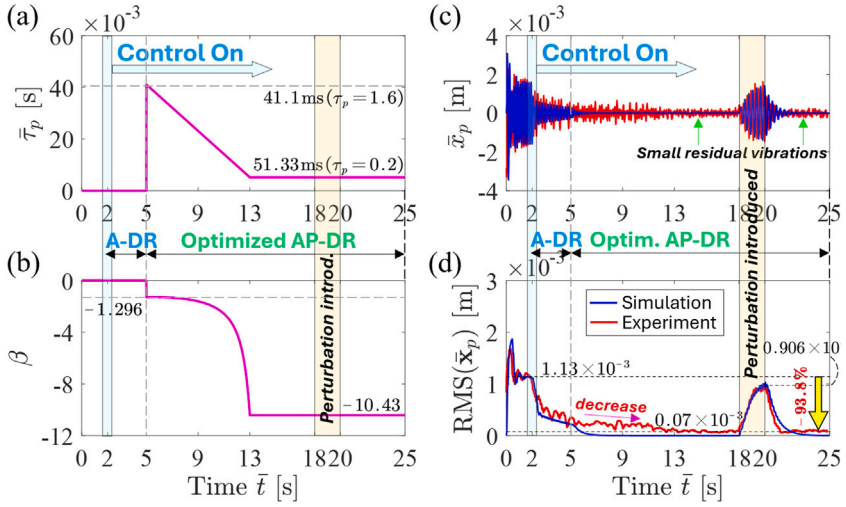

Fig. 16. Verification of enhanced complete vibration suppression by optimizing the AP-DR for $\bar{\omega} = 6$ Hz. (a, b). Variations of $(\bar{\tau}_p, \beta)$ versus $\bar{t}$. (c). Time history of $\bar{x}_p$. (d). RMS of $\bar{x}_p$ grids sampled at last 400 time steps before $\bar{t}$. Excitation force is slightly perturbated with $\bar{f}_e = 4\sin(12\pi\bar{t}) + 0.4\sin(6.56\pi\bar{t}) \times (18\text{ s} < \bar{t} < 20\text{ s})$. A-DR is with $\beta = 0$, and $(\bar{\tau}_p, \beta)$ for the AP-DR follow (a, b).

of both the absorber and the primary structure. The newly introduced feedback forces related to the primary structure provide two additional control parameters (β, τ_p) to manipulate system responses. Beneficially, the values of (β, τ_p) do not affect the tuning of the classical two (g, τ_a) to achieve complete vibration suppression since the corresponding feedback forces are zero when the primary is completely settled. Hence, H_∞ optimization can be achieved by solely tuning (β, τ_p), which is decoupled from tuning (g, τ_a), thus reducing the optimization complexity. Comparisons are then conducted between the resulting AP-DR with (17) and the classical A-DR with (7) to demonstrate the strength of the hybrid control logic.

First, system stability must be guaranteed for a controlled system. Given a frequency where to achieve complete vibration suppression, (g, τ_a) are determined so that stable regions of (β, τ_p) can be non-conservatively determined as per stability boundaries. Such stable regions also confine the search interval of (β, τ_p) to reduce optimization computations. However, analytically determining the global optimum of (β, τ_p) is inoperable due to the independence between stability and frequency responses. Alternatively, we show that local minima of the amplitude of the highest resonance peak, denoted as h, exist when fixing one of (β, τ_p) while sweeping the other. Based on this, analytical conditions can be established in two categories to seek numerical solutions: one is the equal-peak feature, and the other is the minimum condition of a single peak. To reduce calculations, we iteratively solve the optimum β at each τ_p grid, which avoids multiple solutions and reduces the number of variables and transcendental effects. We show that an optimized AP-DR can significantly reduce h compared with the A-DR.

On the other hand, the complete vibration suppression performance in terms of response speed and width of antiresonance valley at the tuning frequency, related to the optimized AP-DR, are evaluated by the two indices $(\delta_{dom}, \delta_{wa})$ defined in (29). We show that pursuing an extremum reduction of h can be unfavorable since it can unduly increase δ_{dom} and decrease δ_{wa} so that the complete vibration suppression cannot be practically implemented. However, there exist regions of (β, τ_p) where such two indices can both be enhanced while keeping h desirably small compared with those in the A-DR case. Thus, by properly optimizing (β, τ_p), complete vibration suppression can be significantly enhanced while significantly reducing h. In addition, the optimized AP-DR extends the operable low-frequency band compared with the A-DR. All claimed benefits of the optimized AP-DR are experimentally verified, resulting in at least 13.2% extension of the operable low-frequency band, a much shorter settling time, 67.2% reduction of vibrations excited by perturbations at resonance frequencies, and 56% reduction of residual vibrations, which finally leads to an up to 93.8% reduction of vibrations compared with the passive absorber to achieve complete vibration suppression even around the natural frequency of the absorber. In practical applications, compared with the classical A-DR, the AP-DR additionally requires the online states of the primary structure, which, however, will not significantly increase hardware requirements, as aforementioned in Remark 1. The resulting reduced resonance peaks and enhanced complete vibration suppression performance can well handle the cases where vibrations on the primary have multiple frequency components. For instance, when suppressing the vibrations on a gearbox at a given frequency, each gear inside with eccentric mass and different rotating speeds can be a vibration source of different frequencies.

CRediT authorship contribution statement

Yifan Liu: Writing – review & editing, Writing – original draft, Conceptualization. **Bo Yan:** Writing – review & editing, Funding acquisition. **Li Cheng:** Writing – review & editing, Supervision, Resources, Project administration.

Declaration of competing interest

The authors declare that they have no known competing financial interests or personal relationships that could have appeared to influence the work reported in this paper.

Acknowledgments

This work is supported by the National Natural Science Foundation of China under grant nos. 52422504 and 52175125.

Appendix

The SIMULINK-based simulation models, simulation results, and video recordings of experiments in Section 7 can be found at https://bit.ly/3OMRFi0.

Data availability

Data will be made available on request.

References

[1] Frahm H. Device for damping vibrations of bodies. 989, 1911.
[2] Filipovic D, Olgac N. Torsional delayed resonator with velocity feedback. IEEE/ASME Trans Mechatronics 1998;3(1):67–72.
[3] Olgac N, Elmali H, Vijayan S. Introduction to the dual frequency fixed delayed resonator. J Sound Vib 1996;189(3):355–67.
[4] Olgac N, Holm-Hansen B. A novel active vibration absorption technique: delayed resonator. J Sound Vib 1994;176(1):93–104.
[5] Olgac N, Elmali H, Hosek M, Renzulli M. Active vibration control of distributed systems using delayed resonator with acceleration feedback. J Dyn Syst Meas Control 1997;119(3):380–9.
[6] Elmali H, Renzulli M, Olgac N. Experimental comparison of delayed resonator and PD controlled vibration absorbers using electromagnetic actuators. J Dyn Syst Meas Control 2000;122(3):514–20.
[7] Vyhlídal T, Pilbauer D, Alikoc B, Michiels W. Analysis and design aspects of delayed resonator absorber with position, velocity or acceleration feedback. J Sound Vib 2019;459:114831.
[8] Olgac N. Delayed resonators as active dynamic absorbers. 1995.
[9] Nia PM, Sipahi R. Controller design for delay-independent stability of linear time-invariant vibration systems with multiple delays. J Sound Vib 2013;332(14):3589–604.
[10] Vyhlídal T, Olgac N, Kučera V. Delayed resonator with acceleration feedback–complete stability analysis by spectral methods and vibration absorber design. J Sound Vib 2014;333(25):6781–95.
[11] Sun Y, Xu J. Experiments and analysis for a controlled mechanical absorber considering delay effect. J Sound Vib 2015;339:25–37.
[12] Xu J, Sun Y. Experimental studies on active control of a dynamic system via a time-delayed absorber. Acta Mech Sin 2015;31:229–47.
[13] Kammer AS, Olgac N. Delayed-feedback vibration absorbers to enhance energy harvesting. J Sound Vib 2016;363:54–67.
[14] Karama M, Hamdi M, Habbad M. Energy harvesting in a nonlinear energy sink absorber using delayed resonators. Nonlinear Dynam 2021;105(1):113–29.
[15] Pilbauer D, Vyhlídal T, Olgac N. Delayed resonator with distributed delay in acceleration feedback—design and experimental verification. IEEE/ASME Trans Mechatronics 2016;21(4):2120–31.
[16] Kučera V, Pilbauer D, Vyhlídal T, Olgac N. Extended delayed resonators–design and experimental verification. Mechatronics 2017;41:29–44.
[17] Liu Y, Olgac N, Cheng L. Delayed resonator with multiple distributed delays–considering and optimizing the inherent loop delay. J Sound Vib 2024;576:118290.
[18] Pilbauer D, Vyhlídal T, Michiels W. Optimized design of robust resonator with distributed time-delay. J Sound Vib 2019;443:576–90.
[19] Eris O, Alikoc B, Ergenc AF. A new delayed resonator design approach for extended operable frequency range. J Vib Acoust 2018;140(4):041003.
[20] Zhang X, Xu J, Ji J. Modelling and tuning for a time-delayed vibration absorber with friction. J Sound Vib 2018;424:137–57.
[21] Sinou J-J, Chomette B. Active vibration control and stability analysis of a time-delay system subjected to friction-induced vibration. J Sound Vib 2021;500:116013.
[22] Cai J, Gao Q, Liu Y, Olgac N. Control design, analysis, and optimization of fractional-order delayed resonator for complete vibration absorption. J Sound Vib 2024;571:118083.
[23] Cai J, Liu Y, Gao Q, Chen Y. Spectrum-based stability analysis for fractional-order delayed resonator with order scheduling. J Sound Vib 2023;546:117440.
[24] Kuře M, Bušek J, Boussaada I, Michiels W, Niculescu S-I, Vyhlídal T. Robust delayed resonator with acceleration feedback—design by double root assignment and experimental validation. J Sound Vib 2024;576:118261.
[25] Šika Z, Krivošej J, Vyhlídal T. Three dimensional delayed resonator of Stewart platform type for entire absorption of fully spatial vibration. J Sound Vib 2024;118154.
[26] Šika Z, Vyhlídal T, Neusser Z. Two-dimensional delayed resonator for entire vibration absorption. J Sound Vib 2021;500:116010.
[27] Vyhlídal T, Michiels W, Neusser Z, Bušek J, Šika Z. Analysis and optimized design of an actively controlled two-dimensional delayed resonator. Mech Syst Signal Process 2022;178:109195.
[28] Jenkins R, Olgac N. Real-time tuning of delayed resonator-based absorbers for spectral and spatial variations. J Vib Acoust 2019;141(2):021011.
[29] Olgac N, Jenkins R. Actively tuned noncollocated vibration absorption: An unexplored venue in vibration science and a benchmark problem. IEEE Trans Control Syst Technol 2020;29(1):294–304.
[30] Saldanha A, Michiels W, Kuře M, Bušek J, Vyhlídal T. Stability optimization of time-delay systems with zero-location constraints applied to non-collocated vibration suppression. Mech Syst Signal Process 2024;208:110886.
[31] Silm H, Kuře M, Bušek J, Michiels W, Vyhlídal T. Spectral design and experimental validation of noncollocated vibration suppression by a delayed resonator and time-delay controller. IEEE Trans Control Syst Technol 2023.
[32] Cai J, Gao Q, Zhu S. Experimental investigation of time-delayed control for enhanced performance in a high-static-low-dynamic-stiffness vibration isolation system. IEEE/ASME Trans Mechatronics 2024.
[33] Gao Y, Wang L. Broad bandgap active metamaterials with optimal time-delayed control. Int J Mech Sci 2023;254:108449.
[34] Liu Y, Cai J, Olgac N, Gao Q. A robust delayed resonator construction using amplifying mechanism. J Vib Acoust 2023;145(1):011010.
[35] Liu Y, Cheng L. A high-static-low-dynamic-stiffness delayed resonator vibration absorber. Commun Nonlinear Sci Numer Simul 2025;140:108299.
[36] Sun X, Zhang S, Xu J. Parameter design of a multi-delayed isolator with asymmetrical nonlinearity. Int J Mech Sci 2018;138:398–408.
[37] Wang F, Sun X, Meng H, Xu J. Time-delayed feedback control design and its application for vibration absorption. IEEE Trans Ind Electron 2020;68(9):8593–602.
[38] Yan B, Wang X, Ma H, Lu W, Li Q. Hybrid time-delayed feedforward and feedback control of lever-type quasi-zero-stiffness vibration isolators. IEEE Trans Ind Electron 2024;71(3):2810–9.
[39] Bahnasy TA, Amer T, Abohamer M, Abosheiaha H, Elameer A, Almahalawy A. Stability and bifurcation analysis of a 2DOF dynamical system with piezoelectric device and feedback control. Sci Rep 2024;14(1):26477.
[40] Bahnasy TA, Amer T, Almahalawy A, Abohamer M, Abosheiaha H, Elameer A. A chaotic behavior and stability analysis on quasi-zero stiffness vibration isolators with multi-control methodologies. J Low Freq Noise Vib Act Control 2025;14613484251316934.
[41] Lu Q, Wang P, Liu C. An analytical and experimental study on adaptive active vibration control of sandwich beam. Int J Mech Sci 2022;232:107634.
[42] Zhang Y, Sun W, Zhang H, Du D, Xu K. Active vibration control of fluid-conveying pipelines: Theoretical and experimental studies. Int J Mech Sci 2024;270:109106.
[43] Amer T, Abdelhfeez S, Elbaz RF. Modeling and analyzing the motion of a 2DOF dynamical tuned absorber system close to resonance. Arch Appl Mech 2023;93(2):785–812.
[44] Chang Y, Zhou J, Wang K, Xu D. A quasi-zero-stiffness dynamic vibration absorber. J Sound Vib 2021;494:115859.
[45] Sheng H, He M-X, Ding Q. Vibration suppression by mistuning acoustic black hole dynamic vibration absorbers. J Sound Vib 2023;542:117370.
[46] Ewins D. Control of vibration and resonance in aero engines and rotating machinery–an overview. Int J Press Vessels Pip 2010;87(9):504–10.
[47] Brock JE. A note on the damped vibration absorber. Trans ASME, J Appl Mech 1946;13–4:A–284.
[48] Den Hartog JP. Mechanical vibrations. Courier Corporation; 1985.
[49] Anh N, Tuan VA, Thang PM, Linh N. Extension of the fixed point theory to tuned mass dampers with piezoelectric stack energy harvester. J Sound Vib 2024;581:118411.
[50] Gutierrez Soto M, Adeli H. Tuned mass dampers. Arch Comput Methods Eng 2013;20:419–31.
[51] Habib G, Detroux T, Viguié R, Kerschen G. Nonlinear generalization of Den Hartogś equal-peak method. Mech Syst Signal Process 2015;52:17–28.
[52] Li Z, Xu K, Wang Z, Bi K, Qin H, Giaralis A. Analytical design of non-grounded tuned mass-damper-inerter for base-excited structures. Int J Mech Sci 2024;276:109394.
[53] Liu Y, Cheng L. Exact H ∞ optimization of dynamic vibration absorbers: Univariate-polynomial-based algorithm and operability analysis. Appl Math Model 2025;139:115812.
[54] Nishihara O, Asami T. Closed-form solutions to the exact optimizations of dynamic vibration absorbers (minimizations of the maximum amplitude magnification factors). J Vib Acoust 2002;124(4):576–82.
[55] Yang F, Sedaghati R, Esmailzadeh E. Vibration suppression of structures using tuned mass damper technology: A state-of-the-art review. J Vib Control 2022;28(7–8):812–36.
[56] Chatterjee S. Optimal active absorber with internal state feedback for controlling resonant and transient vibration. J Sound Vib 2010;329(26):5397–414.
[57] Cheung Y, Wong WO, Cheng L. Design optimization of a damped hybrid vibration absorber. J Sound Vib 2012;331(4):750–66.
[58] Li B, Ouyang H, Zhang J-F, Jiang Y-J, Hu Z-G. H ∞ control-based optimization design for active and passive dynamic vibration absorber. J Vib Eng Technol 2024;12(1):783–96.
[59] Zhao G, Raze G, Paknejad A, Deraemaeker A, Kerschen G, Collette C. Active tuned inerter-damper for smart structures and its H ∞ optimisation. Mech Syst Signal Process 2019;129:470–8.
[60] Qiao M, Liu L, Cai B, Wang P, Zhao G. Experimental study on an enhanced integral force feedback controller for active damping. J Low Freq Noise Vib Act Control 2024;14613484241244673.
[61] Zhao G, Paknejad A, Raze G, Deraemaeker A, Kerschen G, Collette C. Experimental study on active tuned inerter-dampers: Application to active damping using force feedback. J Sound Vib 2021;514:116443.
[62] Meng H, Sun X, Xu J, Wang F. The generalization of equal-peak method for delay-coupled nonlinear system. Phys D: Nonlinear Phenom 2020;403:132340.
[63] Meng H, Sun X, Xu J, Wang F. Establishment of the equal-peak principle for a multiple-DOF nonlinear system with multiple time-delayed vibration absorbers. Nonlinear Dynam 2021;104:241–66.
[64] Meng H, Sun X, Xu J, Wang F. Multimodal vibration suppression of nonlinear Euler–Bernoulli beam by multiple time-delayed vibration absorbers. Meccanica 2021;56(10):2429–49.

[65] Wang L, Shi W, Zhou Y, Zhang Q. Semi-active eddy current pendulum tuned mass damper with variable frequency and damping. Smart Struct Syst 2020;25(1):65–80.
[66] Sun R, Wong W, Cheng L. Tunable electromagnetic shunt damper with opposing magnets configuration. Smart Mater Struct 2020;29(11):115034.
[67] Sun R, Wong W, Cheng L. Hybrid electromagnetic shunt damper with Coulomb friction and negative impedance converter. Int J Mech Sci 2022;230:107552.
[68] Sun R, Wong W, Cheng L. A tunable hybrid damper with Coulomb friction and electromagnetic shunt damping. J Sound Vib 2022;524:116778.
[69] Marton L, Lantos B. Modeling, identification, and compensation of stick-slip friction. IEEE Trans Ind Electron 2007;54(1):511–21.
[70] Vyhlidal T, Zitek P. Mapping based algorithm for large-scale computation of quasi-polynomial zeros. IEEE Trans Autom Control 2009;54(1):171–7.
[71] Cheung Y, Wong WO. H-infinity optimization of a variant design of the dynamic vibration absorber—revisited and new results. J Sound Vib 2011;330(16):3901–12.
[72] Hale JK, Infante EF, Tsen F-SP. Stability in linear delay equations. J Math Anal Appl 1985;105(2):533–55.
[73] Olgac N, Sipahi R. An exact method for the stability analysis of time-delayed linear time-invariant (LTI) systems. IEEE Trans Autom Control 2002;47(5):793–7.